Published in final edited form as:
Neuron. 2020 October 14; 108(1): 145–163.e10. doi:10.1016/j.neuron.2020.08.006.

The neuroanatomical ultrastructure and function of a biological ring attractor

Daniel B. Turner-Evans[1,*], **Kristopher T. Jensen**[#1,2], **Saba Ali**[#1], **Tyler Paterson**[#1], **Arlo Sheridan**[#1], **Robert P. Ray**[1], **Tanya Wolff**[1], **Scott Lauritzen**[1], **Gerald M. Rubin**[1], **Davi Bock**[1,3], **Vivek Jayaraman**[1,*]

[1]Janelia Research Campus, Howard Hughes Medical Institute, Ashburn, VA 20147

[2]Computational and Biological Learning Lab, Department of Engineering, University of Cambridge, Cambridge, UK

[3]Department of Neurological Sciences, University of Vermont Larner College of Medicine, Burlington, VT 05405

[#] These authors contributed equally to this work.

SUMMARY

Neural representations of head direction have been discovered in many species. Theoretical work has proposed that the dynamics associated with these representations are generated, maintained, and updated by recurrent network structures called ring attractors. We evaluated this theorized structure-function relationship by performing electron microscopy-based circuit reconstruction and RNA profiling of identified cell types in the heading direction system of *Drosophila melanogaster*. We identified motifs that have been hypothesized to maintain the heading representation in darkness, update it when the animal turns, and tether it to visual cues. Functional studies provided support for the proposed roles of individual excitatory or inhibitory circuit elements in shaping activity. We also discovered recurrent connections between neuronal arbors with mixed pre- and post-synaptic specializations. Our results confirm that the *Drosophila* heading direction network contains the core components of a ring attractor while also revealing unpredicted structural features that might enhance the network's computational power.

Introduction

Mammalian head-direction cells provide one of the clearest examples of an internal representation of an animal's relationship to its surroundings (Taube et al., 1990a). The head-direction representation uses visual cues in the environment as a reference, but persists in darkness, where it is updated by self-motion cues (Taube et al., 1990b). This internal representation likely guides navigation behaviors. Indeed, perturbations to the system in rats induce errors in path-integration (Butler et al., 2017; Valerio and Taube, 2012). A large body of theoretical work has addressed conceptual questions about how such a representation of head direction might be generated and updated (Knierim and Zhang,

---

[*]Corresponding authors.

2012). These studies propose that the neuronal population dynamics associated with head-direction representations are maintained by network structures called ring attractors (Skaggs et al., 1995; Zhang, 1996). These recurrent networks, which are ideally suited to encode a circular variable like head-direction, are often schematized as a ring of neurons whose connectivity depends on their directional tuning preferences (Figure 1A). In most model implementations, neurons with similar directional tuning excite each other and those with different tuning inhibit each other (Figure 1A), thereby enabling the generation of a stable pattern of localized activity in any part of the network (Amari, 1977; Ben-Yishai et al., 1995; Wu and Amari, 2005). Recurrent loops with a shift move the activity ‘bump’ around the ring as the animal turns (Figure 1B–D), and the compass-like representation is tethered to the animal’s surroundings through visual inputs, which are used as a reference to guide heading (Figure 1E, 1F). Experimental support for this general theoretical formulation has come from analyses of head-direction cell population activity under a variety of different conditions (Butler et al., 2017; Chaudhuri et al., 2019; Clark and Taube, 2012; Hargreaves et al., 2007; Muir et al., 2009; Peyrache et al., 2015; Taube et al., 1990b; Yoganarasimha et al., 2006). However, different network implementations of this general formulation make distinct assumptions about the connectivity of their constituent neurons (Ben-Yishai et al., 1995; Xie et al., 2002; Zhang, 1996) (for example, Figure 1A–F). Importantly, such assumptions, which dictate exactly how the circuit functions, have been difficult to test in the large mammalian brain. Mammalian head-direction cells are distributed across many brain regions (Taube, 2007) and are as yet not well classified into types, making it challenging to identify and target them reliably.

An internal heading representation with similarities to the mammalian head-direction representation has also been discovered in the fly brain (Seelig and Jayaraman, 2015). Like the mammalian system, this heading representation tethers to visual surroundings and is maintained and updated in darkness. The fly’s experimental advantages —its small brain, identified neurons, genetic tools, and physiological tractability— make it an excellent system to assess the assumptions underlying the function of ring attractor networks (Figure 1A–F). Indeed, there is strong experimental and theoretical evidence from *Drosophila melanogaster* that the representation of heading is implemented by a ring attractor (Green et al., 2017; Kim et al., 2017; Seelig and Jayaraman, 2015; Turner-Evans et al., 2017). A computational model of a ring attractor that assumes recurrent connectivity between heading neurons and neurons that encode both angular-velocity and heading (Figure 1B–D) has been shown to maintain an accurate representation of the fly’s heading when the circuit is driven by realistic velocity inputs (Turner-Evans et al., 2017). This model replicates the dynamics of the fly heading direction network in darkness. Other models have invoked plasticity between visual inputs and heading neurons to suggest how visual and angular velocity information might update the representation in a mutually consistent manner (Figure 1E, 1F) (Cope et al., 2017; Kim et al., 2019).

Importantly, however, these and other models of ring attractor networks in the fly have assumed the circuit’s connectivity based on relatively indirect evidence (Cope et al., 2017; Han et al., 2019; Kakaria and de Bivort, 2017; Kim et al., 2019; Kim et al., 2017; Su et al., 2017; Turner-Evans et al., 2017). For example, the location of pre- and post-synaptic arbors has been inferred from whether neural processes visible in light-microscopic images seem spine- or bouton-like in specific substructures (Hanesch et al., 1989; Lin et al., 2013; Wolff et al., 2015). The hypothesized connectivity of the circuit has then been derived from light-level overlap between the putatively pre- and post-synaptic arbors of neurons, in some cases further supported by GFP-reconstitution-across-synaptic-partners (GRASP) (Xie et al., 2017) and trans-Tango (Omoto et al., 2018) experiments, although the reliability and accuracy of these methods to estimate pairwise connectivity is known to be limited (Lee et al., 2017; Talay et al., 2017). Similarly, measurements of functional connectivity by optogenetic stimulation of a population of one type of neurons and calcium imaging of another (Franconville et al., 2018) can be difficult to interpret within recurrent networks, particularly if the connections are indirect.

In the current study, we used reconstructions based on serial transmission electron microscopy (EM) (Zheng et al., 2018) to determine synaptic connectivity within the neural network underlying the fly's heading representation. To verify that our results are consistent across flies (and across methods), we compared our neural connectivity matrices to those extracted from the recently released fly hemibrain connectome (Scheffer et al., 2020; Xu et al., 2020), which was obtained by using focused ion beam scanning electron microscopy (FIBSEM). We supplemented this connectivity map with cell-type-specific RNA sequencing (RNA-Seq) and fluorescence in situ hybridization (FISH), which allowed us to characterize the expression profiles of the key cellular components of the ring attractor network. We then used this integrated information to quantitatively assess the role of each of the constituent cell types in the ring attractor's dynamics. We found that the structure of the heading direction network contains motifs similar to those proposed in theoretical models. These motifs were hypothesized to maintain the heading representation activity and update it both in the dark and when visual features are present. We tested these ideas using targeted two-photon calcium imaging and thermogenetic perturbations of the constituent neuron types in behaving, head-fixed *Drosophila*. We also found that many neurons have mixed pre- and post-synaptic specializations within their innervations to single brain structures, creating "hyper-local" recurrent loops that may allow local computations to supplement the role of recurrence at the network level. Moreover, while many implementations of ring attractor networks rely on distinct units that provide local excitation and long-range inhibition to shape activity into one stable bump, consistent with our results, we found apparent redundancy in these structural elements. Both local excitation and long-range inhibition appear to be carried out by multiple classes of neurons. Taken together, our results provide new structural and functional insights into how a small biological ring attractor network allows an animal to maintain an accurate internal sense of direction.

Results

The fly's heading is topographically represented in the toroid-shaped ellipsoid body (EB), a structure within a brain region called the central complex (Figure 1G). The representation manifests as a localized 'bump' of population activity in the so-called E-PG neurons (see STAR Methods for notes on nomenclature) (Seelig and Jayaraman, 2015). Neurons in the E-PG population together tile the EB, with each neuron's arbors occupying a single ~22.5° wedge of the EB (Wolff et al., 2015). E-PG neurons in nearby wedges are tuned to similar heading directions and those in angularly distant wedges to different heading directions, resulting in a complete topographical representation across the circumference of the EB. To observe E-PG activity, we placed tethered, walking flies on a ball inside a visual virtual reality (VR) setup (Figure 1H). The setup permitted the fly to control its angular orientation relative to visual cues presented (see STAR Methods). We exposed the fly's brain and performed two-photon laser scanning microscopy using the genetically encoded calcium indicator, GCaMP6f (Chen et al., 2013) (see STAR Methods), which we expressed selectively in E-PG neurons (Figure 1I). As in previous studies, we characterized E-PG population dynamics by computing and tracking the population vector average of E-PG activity (Figure 1I) in flies walking in darkness and in closed-loop VR in simple, single-stripe visual environments (Fisher et al., 2019; Green et al., 2017; Green et al., 2019; Seelig and Jayaraman, 2015; Turner-Evans et al., 2017). The E-PG bump tracked the fly's heading in darkness and, more reliably, in closed loop visual VR conditions (Figure 1J, Figure S1A, S1B). We also quantified the stability of the heading representation over time, confirming that the bump reliably tracked the heading over a 5 s sliding window across the trial (Figure S1C–E, see STAR Methods). Having confirmed that the heading representation accurately integrates the fly's heading, we sought to characterize the cell types and network motifs that together generate the E-PG bump and its ring-attractor-like dynamics.

Cellular- and synaptic- resolution network motifs underlying the ring attractor network

We first focused on uncovering —at cellular and synaptic resolution— the motifs that together constitute the core of the ring attractor network (Figure 1A–F). For this, we relied on a synaptic-resolution whole-brain EM dataset (Zheng et al., 2018) (Figure 2A). Note that the resolution of our data did not permit the identification of electrical synapses. We reconstructed several neurons of each of the 'columnar' cell types that connect localized areas within two of the brain regions where the heading representation has been studied previously in the fly: the EB and protocerebral bridge (PB) (Figure S2A) (Green et al., 2017; Seelig and Jayaraman, 2015; Turner-Evans et al., 2017). We also reconstructed a few representative examples of 'tangential' neurons that arborize throughout either the EB or the PB. We reconstructed these selected neurons to morphological completion in both of these brain areas and annotated all synaptic contacts between the reconstructed neurons (Figure 2B, see STAR Methods). In all cases, we validated our conclusions by analyzing the connectivity between the same sets of neurons in the FIBSEM-based hemibrain connectome (Scheffer et al., 2020; Xu et al., 2020).

We focused on all the known 'columnar' neuron types (E-PG, P-EN1, P-EN2, P-EG) that link specific EB wedges with corresponding columns in the PB, and on a subset of known 'tangential neurons' (ring and Δ7 neurons) within the specific sub-regions of the EB and PB that were innervated by the columnar neurons (Figure 2C–D; also see note on nomenclature in STAR Methods) (Hanesch et al., 1989; Lin et al., 2013; Wolff et al., 2015; Wolff and Rubin, 2018). Based on the stereotyped morphologies and tiled projection patterns of each of these cell types within the EB and PB, we expected that the connectivity patterns we uncovered within these selected sub-regions would generalize to the other wedges and columns in the EB and PB, something that awaits confirmation in the hemibrain connectome (manuscript in preparation). We marked every pre- and post-synaptic site in each neuron that we traced and constructed connectivity matrices for each region (Figure 2E). While this approach allowed us to identify how often these chosen neurons synapsed onto one another, it still left many partners unidentified. To check the completeness of our synapse partner identification, we therefore looked at the percent of inputs and outputs that were labeled (See STAR Methods for synapse distribution protocol, Figure S3). We could identify approximately 60% of the total inputs in the PB and EB, approximately 40% of the inputs in the NO, and approximately 40% of all outputs across regions. The unidentified connections are to neurons that we did not reconstruct, but that should become clearer after analysis of the central complex network in the hemibrain connectome (manuscript in preparation).

Next, to determine the signs of the connections between identified partners —that is, whether synaptic connections are excitatory or inhibitory— we performed RNA-Seq on each cell type that we could target specifically with GAL4 driver lines (Figure 2F–H, Figure S2B; see STAR Methods) (Aso et al., 2019; Davis et al., 2019). For some cell types, we also used FISH in parallel to confirm the likely neurotransmitter (Long et al., 2017; Meissner et al., 2019). Most cell types appear to express only one neurotransmitter and likely express receptors for most, if not all, neurotransmitters (Davis et al., 2019).

Both receptor and neurotransmitter identity are needed to infer the likely sign of a synaptic connection between two neurons. Consistent with past work (Davis et al., 2019), in all cell types that we examined, we identified only a single neurotransmitter for which all associated genes were consistently expressed across samples and at levels comparable to or greater than the whole brain data. E-PGs, P-EGs, P-EN1s, and P-EN2s all express both biosynthetic acetyl transferase (ChAT) and vesicular transporter (VChAT) at levels comparable to the whole brain data, identifying them as cholinergic (Figure 2F, 2H, Figure S4A). The subclass of ring neurons that we targeted, likely visual neurons, expressed Gad1, the enzyme that produces GABA (adjusted p = 6.3E-5 with respect to the whole brain data), identifying them as GABAergic (Figure 2G, see Supplemental Information for neuropeptide signaling, Figure S4B) (Enell et al., 2007; Homberg et al., 1999; Kahsai et al., 2012; Martin-Pena et al., 2014; Zhang et al., 2013). The Δ7s expressed VGlut, marking them as glutamatergic (Figure 2F, adjusted p = 3.1E-2) (Daniels et al., 2008). Note that although VGlut expression is detectable in two of four E-PG samples, it is detected at much lower levels than seen in the glutamatergic Δ7 neurons or in the whole-brain data (Figure 2F, Figure S4A). Similarly, the expression levels of both the biosynthetic Gad1 and vesicular transporter VGAT are substantially lower in all E-PG neurons than those seen in the GABAergic ring neurons or in whole brain data. Receptor identity will be discussed in the following sections. Having measured the synaptic connectivity matrix for the key components of the EB-PB heading direction network, and having gained some insight into their synaptic and cellular properties from RNA-Seq and FISH, we next asked how these different cell types and motifs might underlie specific properties of the ring attractor network.

E-PG neuron output is essential to the maintenance of the heading representation

The fly ring attractor network is thought to enable the formation of a single, stable bump of activity through local excitation and near-uniform inhibition (Kim et al., 2017). Local excitation reinforces activity at the bump location while long-range inhibition suppresses activity in neurons with different heading tuning. In prior work (Turner-Evans et al., 2017), we had suggested that the E-PG neurons are the center of the ring attractor network, and that their role in driving excitatory recurrent loops was essential to the generation of a stable heading representation (Figure 3A). We further suggested that the Δ7 neurons might provide the necessary long-range inhibition. Here, we test these assumptions at the level of connectivity and functional activity in the E-PG and Δ7 neurons.

Our data revealed that E-PG neurons (Figure 3B, 3C) are cholinergic (likely excitatory, Figure 2F), and are the sole columnar neuron type that both receives synaptic input in the EB and provides a significant number of synaptic outputs to neurons in the PB (E-PG: 872 ± 80 T-shaped presynaptic transmitter release sites, or T-bars, per neuron in the PB; P-EN1: 1; P-EN2: 3; P-EG: 0). These data, which are corroborated by the FIBSEM connectome (manuscript in preparation), are consistent with the E-PG neuron type's proposed role as the primary, excitatory neural population in the fly ring attractor network. In addition, examining the connectivity between E-PGs within the EB (Figure 3D, matching FIBSEM-based connectivity matrix shown in Figure S5A), we found that the neurons within a given wedge are not purely post-synaptic (Lin et al., 2013), but rather make synapses onto one another (regions along the diagonal in the connectivity matrix), consistent with the locally excitatory connectivity predicted by many ring attractor models (Kim et al., 2017), an idea also supported by RNA-Seq analysis of the E-PGs, which revealed that they express nicotinic acetylcholine receptors (Figure 3E).

However, a key question about the E-PG neurons is whether their compass-like activity is entirely derived from their inputs or whether they are themselves required to generate these dynamics. If the heading representation is inherited from other cell types that provide input to the E-PG population, blocking E-PG outputs should leave their heading tuning unimpaired. By contrast, if E-PGs themselves are an important hub in the heading direction network, as has been strongly suggested previously (Kim et al., 2017; Turner-Evans et al., 2017), blocking the E-PG outputs should destroy their heading tuning. To answer this question, we expressed both GCaMP6f and the temperature-sensitive mutation of the *Drosophila* dynamin orthologue, shibire^{ts1} (shi^{ts})(Kitamoto, 2002), which blocks vesicle endocytosis and thus synaptic transmission at elevated temperatures, in the E-PGs and measured their Ca^{2+} activity at both permissive and restrictive temperatures. At permissive temperatures, one bump of activity was clearly visible and tracked the animal's movements (Figure 3F, top). In contrast, at higher temperatures, the E-PG activity in the entire EB instead rapidly increased when the animal turned and decreased shortly thereafter (Figure 3F bottom, Figure S5B–E). Average EB E-PG activity, which was higher in visual conditions than in darkness (Figure S5F), switched to being significantly lower under visual conditions at the restrictive temperature (Figure S5G), a phenomenon that we discuss in the section on ring neuron inputs to the compass. Perhaps most importantly, the magnitude of the population vector average (PVA, a measure of the degree of localization of E-PG activity) dropped drastically across flies at the restrictive temperature (Figure 3G), suggesting that the E-PGs are in fact required to generate compass-like activity dynamics.

The Δ7 neurons stabilize the heading representation by inhibiting E-PG neurons

Long-range inhibition has been a necessary stabilizing feature of all ring attractor networks (Figure 4A), including those proposed for the fly heading direction network (Kakaria and de Bivort, 2017; Kim et al., 2017; Turner-Evans et al., 2017). A prominent candidate for this inhibition has been the Δ7 class of neurons (Heinze and Homberg, 2007; Wolff et al., 2015), which have been shown to functionally inhibit the E-PG population in the PB (Franconville et al., 2018). We first asked if this functional inhibition arises from direct synapses between individual Δ7 neurons onto E-PG neurons. Our EM reconstructions confirmed that E-PGs indeed receive synapses from Δ7 neurons (Figure 4B–D). Importantly, as is clear from more fully reconstructed Δ7 neurons from the FIBSEM connectome (Figure 4E and Figure S6A), and from both the FAFB connectivity matrix (Figure 4D) and the matching matrix based on the FIBSEM connectome (Figure S6B), Δ7 neurons do not synapse onto the E-PG neurons that they themselves receive input from, a difference from our simple schematic (Figure 4A). Our FISH (Figure 4F) and RNA-Seq (Figure 2F) analyses both confirmed previous results suggesting that the Δ7s were glutamatergic (Daniels et al., 2008). In the fly, glutamate can bind to many different types of receptors on downstream partners. NMDA and some mGluR receptors are believed to lead to excitatory responses, while GluClα receptors lead to inhibitory responses (Liu and Wilson, 2013; Xia et al., 2005). The RNA-Seq data revealed GluClα mRNA expression in the E-PG neurons (Figure 3E, Figure S4C, adjusted $p = 0.39$), raising the possibility that GluC1α channels underlie their inhibition by the Δ7 population (Franconville et al., 2018), although we also observed expression of Nmdar1 and Nmdar2 mRNA (adjusted $p = 0.55, 0.28$, respectively). Other glutamate-gated channels had much lower levels of expression (Figure S4C). Consistent with the columnar specificity of their pre- and post-synaptic specializations (Heinze and Homberg, 2007; Wolff et al., 2015) (Figure 4E and Figure S6A), we found that Δ7 neurons synapse selectively onto only the subset of E-PGs within one column in the PB (upper left quadrant of the connectivity matrices in Figure 4D and Figure S6B) and receive broad input from the E-PGs away from that region (lower right quadrants of connectivity matrices in Figure 4D and Figure S6B). Overall, the connectivity and RNA-Seq data are consistent with Δ7s putatively inhibiting those E-PGs that correspond to angular orientations distant from the current orientation.

We also discovered that the Δ7s synapse strongly onto one another (Figure 4D and Figure S6B, upper right quadrant), indicating that these neurons may play a much more nuanced computational role than their light-level anatomy suggests. Unfortunately, our RNA-Seq results for the receptors expressed by Δ7 neurons were inconclusive, with relatively weak signatures of both GluClα and mGluR (Figure S4C).

In many ring attractor models, a single activity bump is ensured by assuming that active head-direction neurons (in our case, E-PG neurons) inhibit others with distant angular orientation tuning preferences. If the Δ 7 population performs such a role, we would expect these neurons to be most active in columns in which the E-PGs are inactive and vice versa. We performed simultaneous two-color imaging of the $Ca^{2}+$ activity of both populations of neurons, labeling one with the green indicator GCaMP6f and one with a red indicator, jRGECO1a (Figure 4G, 4H). As predicted, we found that a bump of Δ7 activity peaked in exactly the opposite angular orientation as the E-PG bump, so that the spatial locations of their respective activity bumps are offset approximately 180° (3.6 ± 0.25 glomeruli, where a spacing of 4 glomeruli would correspond to an offset of 180°) with respect to one another (Figures 4G–J, Figure S6C).

Taken together, the offset between the Δ7 and E-PG bumps, along with the morphology, expression profile, and connectivity of the Δ7 neurons, suggests that the Δ7 neurons provide long-range inhibition that helps maintain a single stable E-PG bump. We used shi^{ts} to perform perturbation experiments to ask if the Δ7s are, in fact, the only source of inhibition in the heading direction network. Specifically, we expressed GCaMP6f in the E-PGs and shi^{ts} in the Δ7s, and measured E-PG Ca^{2+} activity at both permissive and restrictive temperatures. E-PG activity dynamics were as expected in control flies at both low and high temperatures (Figure S6D), with the bump tracking the fly’s virtual orientation. If the Δ7s are the main source of inhibition in the ring attractor network, we would expect that blocking their outputs would cause the overall activity of the E-PGs to increase and the bump shape to be altered, potentially even leading to multiple bumps. However, this is not what we observed. At the restrictive temperature, the bump was less visible than before (Figure 4K–M), and now moved erratically in response to the fly’s movements (Figure 4N–S). Further, although the bump amplitude was lower in these flies as compared to control flies, the bump width remained the same (Figure S6E, S6F). For control flies, at both low and high temperatures, the bump accurately tracked the stripe (Figure 4N, 4P, 4R, 4S; see STAR Methods) as it did for the flies expressing shi^{ts} in the Δ7s at permissive temperatures (Figure 4O, 4Q–S). This tracking was significantly less consistent at the restrictive temperatures (Figure 4Q–S; see STAR Methods). This quantification confirmed that the bump no longer reliably tracks the fly’s movements when Δ7s are inhibited. These observations suggest that while the Δ7 neurons contribute to stabilizing the bump’s movements, other sources of inhibition must act to shape the E-PG activity into one bump. One potential source of such inhibition is the Gall-EB ring neuron population, which has been shown to inhibit the E-PG neurons (Franconville et al., 2018). We did not reconstruct these neurons, but FISH analysis confirms that they are GABAergic as well (Figure S6G).

P-EN1 neurons recurrently connected to E-PGs update the compass during turns

Ring attractor theories typically invoke a distinct class of neurons that are tuned to both angular velocity and heading to update the heading representation as the animal turns in darkness (Figure 1B–D) (Skaggs et al., 1995; Xie et al., 2002; Zhang, 1996). Previous studies provided strong evidence that P-EN1 neurons perform this role in the fly (Green et al., 2017; Turner-Evans et al., 2017). P-EN1 neurons are believed to shift the heading representation around the ring through clockwise and counter-clockwise anatomical offsets (Figure 5A). Light-level characterization and functional connectivity experiments have suggested that P-EN1 neurons receive input from the E-PGs in the PB (Lin et al., 2013; Turner-Evans et al., 2017; Wolff et al., 2015). These neurons then send their outputs to E-PGs in the EB in wedges that are adjacent to those innervated by the E-PGs that provided the same PEN1s with input (Figure 5B) (Green et al., 2017; Turner-Evans et al., 2017; Wolff et al., 2015). We examined whether these connections are direct and synaptic at the level of EM (Figure 5C). In the PB, the E-PGs indeed directly contact the P-EN1s as predicted (lower right quadrant of connection matrices in Figure 5D for FAFB and Figure S7A for

FIBSEM). They also likely inhibit P-EN1s in distant PB glomeruli (and therefore distant angular orientation tuning) through the Δ7 population (Figure S7B, S7C for FAFB and FIBSEM, respectively). In turn, the P-EN1s connect most strongly to anatomically shifted E-PGs in the EB (top left quadrant of connection matrices in Figure 5E for FAFB and Figure S7D for FIBSEM). Interestingly, while there are varying numbers of P-EN1s that link one glomerulus in the PB to one sector in the EB (1 for some columns, 2 for others), the total number of synapses between the P-EN1s and E-PGs in a given sector remains roughly constant (Figure 5F, $p = 0.30$).

We assessed the functional significance of these localized and precisely structured recurrent loops involving the E-PG and P-EN1 neurons by examining bump dynamics when E-PG outputs were blocked using shi^{ts}. As mentioned in a previous section, this manipulation resulted in the entire E-PG population becoming active whenever the animal turned (Figure 3F, Figure S5D, S5E), likely as a result of uniform P-EN1 inputs that were no longer sharpened in their heading tuning by excitation from the E-PGs or by structured inhibition from the Δ7 population (Figure S7B, S7C).

EM reconstruction and synapse annotation also revealed unexpected connections from the E-PGs back to the P-ENs within the EB (Figure 5E and Figure S7D, lower right quadrant). Thus, within the EB, these two classes of neurons form “hyper-local” feedback loops, with pre- and post-synaptic sites located within the same processes in the EB. This may contribute to the persistence of the heading representation in the absence of sensory input (other potential contributing mechanisms are suggested below and in Discussion). Persistent activity in the E-PGs could also be sustained by voltage-gated channels and prevented from running away by inhibitory autoreceptors. Indeed, RNA-Seq of E-PGs reveals expression of several voltage-gated channel-linked genes (Figure 5G, Figure S4D) and mAChR-B mRNA (Figure 3E, Figure S4C adjusted $p = 7.4E-3$). The mammalian homologue of mAChR-B, M4, can act as an inhibitory autoreceptor for acetylcholine (Zhang et al., 2002).

The P-EN1s also arborize within a third brain structure, the noduli (NO). Within this structure, either all of the right half or all of the left half P-EN1s synapse onto one another (quadrants along the diagonal in the connectivity matrices in Figure 5H and Figure S7E), but the function of this local recurrence is not yet clear.

In summary, consistent with previous functional observations (Green et al., 2017; Turner-Evans et al., 2017), the P-EN1 population’s connectivity is consistent with their proposed role in updating the bump position. Further, unexpected local connections between P-EN1s and E-PGs in the EB point to its potential involvement in regulating sustained E-PG activity when the fly is standing still.

Ring neurons tether the compass to visual scenes by selectively inhibiting E-PG neurons

Ring attractor models of head direction networks provide a mechanism for angular integration in the absence of visual cues, but such models (and the real networks that they model) accumulate error over time in darkness. Indeed, the fly compass is more accurate at representing the fly’s heading direction in visual closed-loop conditions than in darkness (Figure 1J, Figure S1A, S1B) (Fisher et al., 2019; Seelig and Jayaraman, 2015). Most head direction network models thus incorporate visual inputs (Figure 6A), and many hypothesize that the synapses between these inputs and compass neurons should be plastic, allowing visual cues to flexibly map onto and thereby tether the heading representation (Figure 1E–F) (Cope et al., 2017; Kim et al., 2019; Knierim et al., 1998; Ocko et al., 2018; Page and Jeffery, 2018).

In *Drosophila*, this tethering is thought to come from a large population of inhibitory ring neurons (Figure 6B) (Hanesch et al., 1989; Homberg et al., 2018; Lin et al., 2013; Omoto et al., 2018; Xie et al., 2017; Young and Armstrong, 2010), an assumption with recent experimental support (Fisher et al., 2019). A potential experimental complication is that there are many types of ring neurons, only some of which are visually tuned (Homberg et al., 2011; Omoto et al., 2017; Omoto et al., 2018; Seelig and Jayaraman, 2013; Shiozaki and Kazama, 2017; Sun et al., 2017). To identify appropriate visual ring neurons to reconstruct in the EM dataset, we performed stochastic labeling of broad ring neuron lines using the FLP-out technique (Figure S8A) (Golic and Lindquist, 1989) (see STAR Methods). This technique allows for individual neurons to be tagged, and here we used it to express GCaMP6f in single neurons in order to monitor their $Ca^{2}+$ activity. This procedure labeled a wide array of morphologically distinct ring neurons, and we measured the activity of each type in response to open-loop rotating stripes (Figure S8A). Consistent with expectations from previous studies (Fisher et al., 2019; Omoto et al., 2017; Seelig and Jayaraman, 2013; Shiozaki and Kazama, 2017; Sun et al., 2017), R4d ring neurons consistently showed strong, ipsilateral responses to rotating stripes presented in open loop in contrast to several other types of ring neurons (Figure S8A). We thus focused our EM reconstruction efforts on the R4d class (Figure 6C), while noting that the R2 ring neurons are also known to be visually responsive (Fisher et al., 2019; Omoto et al., 2017; Seelig and Jayaraman, 2013).

We found that R4d neurons selectively target the E-PGs over the P-EN1s (Figure 6D), consistent with most models of visually tethered ring attractor networks (and with results from the FIBSEM connectome (manuscript in preparation). Insect compass models that incorporate visual input (Cope et al., 2017; Kim et al., 2019) suggest that ring neurons that respond to visual cues at specific orientations should more strongly inhibit E-PGs away from the desired bump location, creating a less-inhibited trough for the bump of activity to settle into for those orientations (Fisher et al., 2019). Such a trough is not visible in the synaptic counts of the ring neurons we reconstructed, nor —as is now clear from the hemibrain connectome (manuscript in preparation)— across the broader ring neuron and E-PG populations. Instead, the number of synapses between the ring neurons and the E-PGs is relatively constant across the sectors of the EB that we reconstructed. The trough may indeed be represented in synapse numbers, but it may not be visible across the limited section of the EB that we traced, or it may instead be represented in the strengths of the synapses but not in their numbers.

A surprise in the EM reconstructions was how heavily R4d ring neurons synapse onto each other (Figure 6E). RNA-Seq of these neurons revealed relatively high expression levels of GABA related receptor genes as compared to the whole brain data (Figure 6F, Figures S4B, adjusted p = 1.9E-19 for Rdl), suggesting that ring neurons are inhibited by GABA and therefore by each other. This hypothesis is consistent with recent observations that combined optogenetic stimulation of individual R2 ring neurons with whole-cell patch clamp electrophysiological recordings of other R2 neurons (Isaacman-Beck et al., 2019). When we compared the calcium activity of the R4d population in darkness to the activity seen in the presence of a single bright stripe moving in open loop, we saw signatures of such inhibition in the R4d population as well (Figure S8B, S8C). The overall level of R4d ring neuron population activity was reduced when the fly was shown a stripe in open loop after a period of darkness (Figure S8D, S8E, $p = 2.5E-4$ for activity minimum). The ring neurons that are most strongly excited by the visual stimulus likely inhibit the others, leading to this overall reduction. Such mutual inhibition might also produce competitive dynamics between ring neurons (Sun et al., 2017).

Although we did not detect any consistent patterns in the synapse counts between the ring neurons and the E-PGs, we did find an indication of structured inhibition in our calcium activity recordings in flies that expressed shi^{ts} in the E-PGs. At the permissive temperature, when a clear bump of E-PG activity could be observed, the amplitude of the bump increased when a fly that had previously been in the dark was shown a closed-loop stripe (Figure S5F). In contrast, at the restrictive temperature, when the E-PGs were more uniformly active throughout the EB, the mean EB activity decreased when the fly was shown a stripe (Figure S5G). Taken together, these results suggest that the inhibition locally decreases at the position of the bump while globally increasing in the EB, which is consistent with a trough-shaped structure of inhibitory weights between the visual ring neurons and the E-PG neurons.

In summary, R4d ring neuron connectivity to the E-PG neurons, and changes in E-PG activity in response to visual stimulation are both in line with predictions made by ring attractor models of visuomotor integration. Further, ring neuron-to-ring neuron connectivity may enable competitive dynamics across the ring neuron population.

Pathway from AOTU to EB tethers the compass to visual features

Although we focused on the R4d ring neurons, multiple classes of ring neurons respond to visual features (Omoto et al., 2017). These neurons all arborize in an ancillary structure known as the bulb (BU). They receive visual inputs from a pathway that is conserved across insects and originates in the photoreceptors and travels through the lamina, medulla, and anterior optic tubercle (AOTU) before reaching the BU (Held et al., 2016; Homberg et al., 2011; Homberg et al., 2003). Lineage-based anatomical studies (Omoto et al., 2017) and photoactivatable-GFP (PA-GFP) uncaging in the BU (Sun et al., 2017) suggest that the TuBu neurons provide visual inputs to the ring neurons in the *Drosophila* BU. Silencing the outputs of the TuBu neurons should therefore “blind” the ring neurons and, in turn, “blind” the compass.

Consistent with previous results (Green et al., 2019), in flies with functional AOTU-BU pathways, E-PG neurons maintained a heading representation that accurately tracked a closed-loop stripe, even at high temperatures (Figure 6G, Figure S9A). We next expressed shi^{ts} in TuBu neurons to silence their output. At permissive temperatures, flies that expressed shi^{ts} in the TuBu neurons showed normal heading-tuned activity in E-PG neurons during closed-loop walking (Figure S9B). At the restrictive temperature, the E-PG population representation was impaired, but tracked heading in darkness with no obvious increases in error relative to the permissive temperature (compare dark periods in left halves of Figure 6G, 6H, and similar circular variance between dark periods in Figure 6I, 6J). However, the situation was completely different when the fly was walking in closed loop with a stripe at the restrictive temperature (Figure 6H, right half). In this condition, errors in tracking heading exceeded those in like conditions at the permissive temperature and, in fact, matched errors expected in darkness (6I bottom, 6J right). We therefore concluded that the pathway from the AOTU to the BU to the E-PGs (via the TuBu and ring neurons) provides visual cue information that is used as a reference by the fly compass, allowing the fly to maintain arbitrary headings within its surroundings. In the absence of input from this pathway, the heading representation is relatively untethered from visual stimuli. Based on what is known about visual projections to the EB, the anterior visual pathway from the AOTU likely encodes many more visual cues than just the ‘ON’ contrast stripes that we use here (Omoto et al., 2017). Thus, these results may generalize to more complex visual scenes involving light and dark patches (Kim et al., 2019; Seelig and Jayaraman, 2013; Sun et al., 2017) and to polarized light (el Jundi et al., 2014; Heinze and Homberg, 2009; Omoto et al., 2017).

The E-PG, P-EG and P-EN2 excitatory loop that maintains the compass bump in darkness

Finally, we reconstructed two additional classes of columnar neurons that are connected to the E-PG and Δ7 neurons, but whose function in the context of ring attractor models is less obvious: P-EG and P-EN2 neurons (Figure 7A–C) (Green et al., 2017; Wolff et al., 2015). Based on light microscopy and RNA-Seq, P-EG neurons seemed like they could provide direct cholinergic (excitatory) feedback to the E-PG neurons, aiding in the bump’s persistence (Kakaria and de Bivort, 2017). However, although the P-EGs get strong direct input from the E-PGs in the PB (see lower right quadrant of connectivity matrices in Figure 7D and Figure S10A for FAFB and FIBSEM, respectively), they do not synapse directly back onto the E-PGs in the EB (upper left section of connectivity matrices in Figure 7E and Figure S10B for FAFB and FIBSEM, respectively). Instead they synapse onto the P-EN2s, which are also cholinergic, and in turn synapse onto the E-PGs (upper middle section and middle left section of connectivity matrices in Figure 7E and Figure S10B for FAFB and FIBSEM, respectively) (note that P-EN2s from each side of the PB are densely interconnected with each other and with angular-velocity-carrying P-EN1s in the NO (Figure 7F)). The P-EGs and P-EN2s therefore form a three-synapse feedback loop with the E-PGs: E-PG to P-EG to P-EN2 and back to E-PG. Any P-EG feedback to the E-PGs is therefore mediated by the P-EN2s in the EB. Indeed, P-EN2 activity in the EB largely matches P-EG activity (Figure 7G). Both populations display one bump of activity that moves around the EB, tracking the animal’s heading (Figure 7H), and the bump’s amplitude weakly correlates with the animal’s velocity for each population (Figure S11A–D). The PVA difference between the two is small, around ¼ of the bump full width at half maximum (Figure 7I, 7J), suggesting that the bump of activity in the two populations directly overlap.

We next tested the possibility that the P-EN2 population mediates the transmission of delayed excitatory feedback from the P-EGs to the E-PGs, potentially reinforcing the persistence of E-PG heading representation activity. We monitored E-PG activity while silencing P-EN2 activity using Gal80 and the inwardly rectifying potassium channel, Kir (see STAR Methods), thereby breaking the P-EG feedback loop. Consistent with the importance of the P-EG input for maintaining E-PG bump strength, the E-PG bump was almost entirely abolished in the dark in flies in which Kir was expressed in the P-EN2 population (Figure 7K). This was true regardless of the animal's rotational velocity (Figure 7L, 7M). Instead, the overall activity in the EB increased as the animal turned (Figure S11E, S11F). Interestingly, the bump was clearly visible and tracked the fly's motions in the presence of a stripe in closed loop (Figure S11G–K), consistent with model predictions and recent experiments suggesting that the bump is shaped by visual input from ring neurons (Cope et al., 2017; Fisher et al., 2019; Kim et al., 2019).

In addition to receiving input from the P-EGs in the EB, the P-EN2s also receive input in the PB. There, they receive weak direct E-PG input but strong Δ7 input (see left quadrants in FAFB and FIBSEM connectivity matrices in Figure 7D and Figure S10A, respectively). Thus, there is also a second loop to the E-PGs. This second loop goes from E-PGs to Δ7s to P-EN2s and back to E-PGs (Figure 7A). This loop anatomically resembles the E-PG and P-EN1 loop and would not excite E-PG neurons in the same location in the EB. Curiously, however, a recent study reported that E-PG and P-EN2 activity in the PB are anticorrelated (Green et al., 2017), which we also observed (data not shown). If projected to the EB, this anticorrelated P-EN2 bump in the PB should translate to a bump in the EB that is offset from the P-EG bump, in contrast to what we observed. However, as described above, the P-EN2s also receive direct synaptic input from the P-EGs in the EB, thus complicating the picture in the EB. The discrepancy between P-EN2 activity in the EB and the PB may be accounted for by electrical isolation of the PB and EB compartments of individual P-EN2 neurons (Figure S11L–O, Supplemental Information). The compartmentalization of P-EN2 activity between the EB and PB raises as-yet-unanswered questions about the functional role of these neurons in the heading direction network.

Similar to the E-PG neurons, the activity of P-EG neurons, which receive considerable synaptic input from E-PGs in the PB, is also offset from the P-EN2 bump in the PB (Figure S11P, S11Q). This offset also matches the difference we see between Δ7 and E-PG activity (Figure 4J). Considering that E-PG neurons provide direct synaptic input to Δ7 neurons, and since those neurons, in turn, make synapses onto P-EN2 neurons, a likely possibility is that the glutamatergic Δ7 neurons excite P-EN2 neurons through excitatory glutamate channels. In contrast, the activity of P-EN1s, whose anatomy is almost identical to the P-EN2s, overlaps with the E-PG activity but is anticorrelated with Δ7 activity. We would therefore expect these neurons to be inhibited by the Δ7s. However, we found no clear difference between glutamate channel mRNA expression in the P-EN1s and P-EN2s (data not shown). Resolving this conundrum will require future experiments that establish the localization of specific glutamate channel types in P-EN1 and P-EN2 to their different arbors in the PB, EB and NO.

In summary, although the P-EN2 offset projection pattern leaves open other possibilities, their role in mediating excitatory feedback from P-EG neurons is likely key to the maintenance of E-PG bump strength in the dark.

Flies lose flexibility in heading if AOTU input or EB-PB network is disrupted

In our imaging experiments in flies walking in visual VR (previous sections), we focused on how disrupting signals from specific cell types in the heading direction network impacted the stability of the E-PG heading representation. These disruptions also impacted the fly's behavior (Figure S12). Recent studies have demonstrated that the E-PG compass is required for the fly to select and maintain arbitrary headings relative to visual cues in its surroundings (Giraldo et al., 2018; Green et al., 2019). Consistent with these results, we observed a distinct change in the fly's fixation preferences when we disrupted the heading representation and its tethering to visual features (Figure S12A, S12C–F; STAR Methods). Control flies displayed individual heading preferences relative to a single stripe that were maintained across trials at high temperatures (Figure S12A, S12B), but there was a wide range of preferences across flies. Note that the observation that this behavior is most clearly manifest at higher temperatures is in line with other stripe fixation experiments in tethered walking flies, most of which have been performed at higher temperatures (Bahl et al., 2013; Green et al., 2019). A similar range of heading preferences was observed at the permissive temperature in flies that expressed shi^{ts} in the E-PG, TuBu, and Δ7 neurons (Figure S12C, S12D, S12F top). In contrast, at the restrictive temperature, we observed these flies all had matching heading preferences, keeping the stripe exclusively in the frontal field of view (Figure S12C, S12D, S12F bottom). Taken together with previous results (Giraldo et al., 2018; Green et al., 2019), we conclude that flies' ability to maintain a stable heading representation and exhibit different heading preferences relative to visual cues in their surroundings relies on an intact EB-PB network that receives visual information from the AOTU-BU pathway via the visual ring neurons.

Discussion

Efforts to model the dynamics of head direction networks have long focused on ring attractors. Although this conceptual framework has been very influential, testing the validity of the structural assumptions and functional predictions made by ring attractor models in biological circuits has been challenging. Here, we applied connectomics, transcriptional profiling, and functional imaging with perturbation of genetically targeted neural populations to examine the structure and function of the neuronal circuits underlying heading direction in the fly. Our results allow us to firmly place several cell types and network motifs from the fly into the context of previous ring attractor models: E-PG neurons construct the heading representation from their inputs; heading-tuned P-EN1 neurons provide angular velocity inputs that update the heading representation when the animal turns; and Δ7 neurons provide inhibition that stabilizes the E-PG heading representation by sculpting P-EN1 activity. We previously invoked the E-PG, P-EN1 and, implicitly, Δ7 neurons in a ring attractor model that captured the observed dynamics of the heading direction network (Figure 8A, see STAR Methods) (Turner-Evans et al., 2017). The weights of this model were tuned without any knowledge of the actual synaptic connections. If we extrapolate the measured synapse counts around the ring to form a complete connectivity matrix of the biological network, the theoretical and the experimentally derived connectivity matrices are similar (Figure 8B). Finally, ring neurons, which are known to bring visual information to the EB in a variety of insects (el Jundi et al., 2014; Heinze and Reppert, 2011; Omoto et al., 2017; Phillips-Portillo, 2012; Seelig and Jayaraman, 2013; Shiozaki and Kazama, 2017; Sun et al., 2017; Vitzthum et al., 2002), make synaptic contacts with E-PG neurons, consistent with recent modeling and experimental work suggesting that the ring neuron population tethers the compass to the fly’s sensory surroundings (Cope et al., 2017; Fisher et al., 2019; Kim et al., 2019).

However, while the theoretical predictions and our biological observations are largely consistent, we also uncovered surprises in the biology that will require further theoretical and experimental work to understand. The long-range inhibition that has been invoked to form a stable bump of activity appears to be split across multiple brain regions and multiple classes of neurons (Figure 8C). The Δ7 neurons cannot be the only source of inhibition in the circuit since the E-PG population organizes into a single bump even if the output of the Δ7 neurons is reduced. GABAergic R4d (and other) visual ring neurons also inhibit much of the E-PG population in the presence of visual stimuli. Further, the Gall-EB ring neuron population provides a source of inhibition onto the E-PG neurons (Franconville et al., 2018). We did not reconstruct these neurons, but FISH analysis confirms that they are GABAergic as well (Figure S6G). Indeed, the cumulative inhibition from multiple classes of ring neurons may account for some of the mutual suppression between E-PG neurons (Kim et al., 2017).

Local excitation also appears to be implemented through multiple classes of neurons (Figure 8D). Within the EB, E-PGs synapse onto one another and onto the P-ENs, which in turn synapse back onto the E-PGs—this local recurrence may enable the fly’s internal compass to perform more smoothly than its limited number of neurons may otherwise permit (see, for example, the ‘stickiness’ in bump movement evident in Figure 10 of (Turner-Evans et al., 2017)). Local excitation also appears to be structured across compartments, with the E-PGs synapsing onto the P-ENs in the PB and the P-ENs synapsing on the E-PGs in the EB. Finally, P-EGs appear to create a potentially slower multi-synaptic feedback loop, receiving input from the E-PGs in the PB and synapsing onto the P-EN2s in the EB which in turn synapse back onto the E-PGs. Overall, the redundancy of local excitation and long-range inhibition may allow the network to maintain heading direction activity in the absence of external input. These network features may also provide a means to stabilize the heading representation in the presence of noisy inputs and inhomogeneous synaptic weights, which can disrupt the function of continuous attractor networks (Burak and Fiete, 2012; Compte et al., 2000; Itskov et al., 2011; Renart et al., 2003; Seeholzer et al., 2019; Wu and Amari, 2005; Wu et al., 2008; Zhang, 1996).

Local connections were not limited to the E-PGs. Instead, they appeared across neuron classes and may lead to local computations within the broader ring attractor network. For example, consistent with previous observations from electron microscopy in locusts (Homberg and Muller, 2016) and from *trans-Tango* experiments in flies (Omoto et al., 2018), we observed synapses between the visual ring neurons. These ring neurons tether the bump to a visual scene. Visual scenes are often complex and dynamic and so inter-ring neuron connections may either form a winner-take-all network that leads one visual feature to dominate, preventing the bump from moving erratically as the scene shifts over time (Figure 8E) or provide a mechanism for gain control that normalizes the total level of inhibition from those ring neurons onto the E-PG neurons. The R4d ring neurons traced here are but one of many classes of ring neurons. Other ring neuron types respond to contralateral visual features, or are linked to sleep, circadian rhythm, nutrients, or the animal’s movements (Donlea et al., 2018; Dus et al., 2013; Liang et al., 2019; Liu et al., 2016; Park et al., 2016; Seelig and Jayaraman, 2013; Shiozaki and Kazama, 2017). If similar connections exist between or across these different ring neuron classes, then they may perform computations amongst or between themselves, preprocessing information rather than acting solely as parallel input streams to the E-PG neurons.

Both the structural and functional results also left several puzzles unsolved and raised new questions. The glutamatergic Δ7 neurons synapse onto many columnar neuron types in the PB that project back to the EB, including the P-EN1, P-EN2, and P-EG populations. Indeed, a primary role of the Δ7s may be to pass the heading representation from the E-PGs to other columnar neurons in the circuit. Many columnar neuron types leave the heading direction network and pass into a structure in the CX known as the fan-shaped body. While we did not trace any of these fan-shaped body neurons, we would predict that they also receive input from the Δ7s (something that is indicated in the FIBSEM connectome (manuscript in preparation)). Of the P-EN1, P-EN2, and P-EG neurons, it appears that the Δ7 neurons inhibit the P-EN1 and P-EG neurons but may excite the P-EN2 neurons. This excitation would create a bump of P-EN2 activity that is perfectly offset from the E-PG bump in the PB. However, because of compartmentalization, the P-EN2 activity in the PB only produces a small shoulder of a bump in the EB. There, the main part of the P-EN2 activity instead appears to be driven by local excitation from the P-EG neurons at the E-PG bump location. The combination of P-EG and P-EN2 neurons feeding back with a delay onto the E-PG neurons in the EB helps maintain the strength of the heading representation in darkness, but we cannot yet explain the functional role of the shoulder of activity and its displacement from the E-PG bump.

Behaviorally, the heading representation has been shown to be required for the fly to select and maintain arbitrary headings relative to visual cues in its surroundings (Giraldo et al., 2018; Green et al., 2019), a result that we replicated here. Whenever the heading representation was altered, the fly only walked directly towards a visual cue. However, we note that behavioral genetics experiments in the fly have also implicated the CX in sleep and nutrient-state-induced modulation of activity (Donlea et al., 2018; Dus et al., 2013; Liang et al., 2019), short-term visual orientation memory (Kuntz et al., 2017; Neuser et al., 2008), long-term visual and thermal place memory (Liu et al., 2006; Ofstad et al., 2011), and body-size-dependent motor control (Krause et al., 2019; Triphan et al., 2010). The role of the EB-PB circuit in such functions is unknown.

At a methodological level, the recent completion of the FIBSEM-based connectome (Scheffer et al., 2020; Xu et al., 2020) allowed us to compare our FAFB-based EM reconstructions and synaptic connectivity matrices with those extracted from the hemibrain connectome. As is evident from a visual comparison of the matching connectivity matrices throughout, the FIBSEM dataset reinforces all the conclusions that we drew from FAFB. We quantified the level of correspondence between the datasets by computing the differences between synaptic connectivity for neurons matched across datasets by type and innervation pattern (Figure S13). As shown for the example of the NO (Figure S13A–D), there are sometimes more connections detected for connections between specific types in one or the other dataset (Figure S13E shows this for different connection types in the NO, EB and PB), but it is rare that there are synaptic connections between neuron types in one dataset that are not found in the other (see Figure S13F for the exceptions). We did find that a few of the finer hyper-local connections within neuron types that we could identify in the FAFB dataset were occasionally absent in FIBSEM. It is important to note that, unlike the FIBSEM connectome, the connectivity examined in this study constitutes only a partial connectome, focused on a specific set of neurons selected because of their likely participation in the fly ring attractor network: the E-PG, Δ7, P-EN1, P-EN2, and P-EG neurons. However, this is not an isolated circuit, and we did not attempt to identify all the upstream and downstream partners of these neurons, an analysis of which should be possible in the hemibrain (manuscript in preparation).

Importantly, the CX and its neurons have been studied not just in other contexts, but also in other insects. Intracellular electrophysiological recordings from CX neurons in a diverse array of insects have discovered topographically-organized visual responses, suggesting the potential involvement of the region in computations ranging from sky-compass-based navigation in locusts (Heinze and Homberg, 2007), monarch butterflies (Heinze and Reppert, 2011), and dung beetles (el Jundi et al., 2015) to optic-flow-based path integration in sweat bees (Stone et al., 2017). Extracellular recording and stimulation in the cockroach CX have also implicated the region in sensory-guided orienting and motor control (Bender et al., 2010; Guo and Ritzmann, 2013; Varga and Ritzmann, 2016). Looking ahead, scaled-up electron microscopic reconstructions of CX networks in different insects (for example, recent EM-guided modeling in the sweat bee CX (Stone et al., 2017)) may enable an exploration of how circuits that are optimized for navigation differ based on the particular sensory statistics, ecological niches and biomechanical constraints of each insect.

Finally, our efforts to link structure to function also highlight the challenges that this task poses. Connectomics is often perceived as providing strong constraints on models of circuit function. However, although this was partly true for the heading direction network, our results also identified unexpected computational mechanisms that the circuit may employ. For example, the profusion of mixed pre- and post-synaptic specializations within single compartments of individual neurons created many more locally recurrent loops between similar and different neuron classes. We cannot yet provide a functional account for such dense recurrence. Future theoretical and experimental work to probe their function may well reveal that the fly brains are more powerful than their numerical simplicity might suggest.

STAR Methods

Nomenclature

The columnar neurons (E-PGs, P-EN1s, P-EN2s, and P-EGs) were each assigned a number and an “R” or an “L”. This number-letter combination refers to the glomerulus in the protocerebral bridge in which they arborize. The bridge can be split into right (“R”) and left (“L”) halves, and each half has nine glomeruli (1–9). 9 is always the outer glomerulus while 1 is the glomerulus in the middle. Hence, from left to right, the numbering goes from L9 to

L1 and then from R1 to R9. Where multiple neurons of a single type arborize in the same glomerulus, an “a,” “b,” or “c” was appended to the name (e.g. E-PG 5Rc). The Δ7s arborize throughout the bridge but were named based on the 2 or 3 glomeruli to which they send axons. Finally, ring neurons were assigned an arbitrary letter label from a–g.

More information on the anatomy and nomenclature of the individual neurons can be found in (Wolff et al., 2015). Briefly, E-PG and P-EG neurons that arborize in glomerulus 5 (right or left) project to the 12 o’clock position in the ellipsoid body. P-EN1s and P-EN2s project to offset positions in the ellipsoid body (10:30 for the right bridge neurons, and 1:30 for the left bridge neurons). This offset is consistent for all similar E-PG/P-EG and P-EN1/P-EN2 pairs.

Experimental protocols

Genotypes

Experiment	Parent #1	Parent #2
FISH	UAS-HaloTag	SS00096
“	“	SS00131
“	“	GR37F06
“	“	VT08135
“	“	SS02238
“	“	SS30295
“	“	SS02232
“	“	SS02233
“	“	SS02191
“	“	SS27853
“	“	GR18A05
FLP-out GCaMP	20XUAS>myrTopHat2>Syn21-OpGCaMP6f-p10 su(Hw) attP8; pGP-JFRC59-13XLexAop2-IVS-NES-jRGECO1a-p10 in su(Hw)attP5; +	pBhsFlp2::PEST; LexA-VT25957;EB1
		pBhsFlp2::PEST; LexA-VT25957;c232
Two color calcium imaging	pGP-JFRC59-13XLexAop2-IVS-p10-GCaMP6f; 20XUAS-IVS-jRGECO1a-p10	LexA-60D05; GR55G08
	“	LexA-55G08; R60D05
	13XLexAop2-IVS-Syn21-OpGCaMP6f-p10 su(Hw) attp40; LexA-37F06 VK22; 20XUAS-IVS-jRGECO1a-10	SS02191
	20XUAS-IVS-Syn21-OpGCaMP6f p10 su(Hw)attP8; LexA-37F06 VK22; 13XLexAop2-IVS-Syn21-jRGECO1a	SS02191
Shi	LexA-VT25957; pJFRC100-20XUAS-TTS-Shibire-ts1-p10 in VK00005, 13xLexA-syn21-syt-OpGCaMP6f-p10 in attP2 (wtB)	SS00096
	“	LexA-60D05; GR55G08
	“	R76B06
Kir	tubP Gal80ts; UAS-kir2.1::GFP	LexA-27F02, LexAOp-jRGECO1a; VT20739

Experiment	Parent #1	Parent #2
	“	LexA-27F02, LexAOp-jRGECO1a; GR12D09
RNA-Seq	10XUAS-IVS-myr::GFP; 10XUAS-IVS-nls-tdTomato	SS000096
	“	SS000131
	“	SS30295
	“	SS02238
	“	SS02191
	“	SS00238
	“	SS02232
	“	SS62862

Simultaneous behavioral and calcium activity recordings of a fly on a ball—All imaging experiments were performed with head-fixed, tethered female flies walking on an air-suspended ball as described in (Seelig et al., 2010). Each fly was first cold anaesthetized and the proboscis fixed with wax to limit brain movement. The fly was then glued to a pin and positioned in an inverted pyramidal metal shim such that the top of the head was exposed while the body was free and visibility only minimally occluded. The head was then glued to the shim and immersed in saline. The cuticle was removed above the brain, along with any fat, and the air sacs and trachea were pinned to the side. Finally, the muscles that run along the top of the esophagus were cut to limit brain movement. The holder was then positioned such that the fly was centered on the ball and could walk freely.

The movements of the ball (a proxy for the walking movements of the fly) were recorded using the fly spherical treadmill system (Seelig et al., 2010). These movements were fed via USB to a PC and both recorded and used to update closed loop visual stimuli as needed (described further below).

Calcium imaging experiments were performed as described in (Turner-Evans et al., 2017). Briefly, a custom two-photon microscope running ScanImage, similar to the one described in (Seelig and Jayaraman, 2015), was used for all experiments. A full description of the filter sets can be found in (Turner-Evans et al., 2017). All imaging was performed using a tunable femtosecond pulsed laser at ~20 mW power, set at 930 nm for one color and 1020 nm for two color experiments. 256 × 256 pixel images were obtained across multiple Z planes to form a volume. The volumes were ~50 μm on a side and consisted of 6 Z planes, each spaced 8 μm apart (for ellipsoid body imaging) or 12 Z planes, each spaced 4 μm apart (for protocerebral bridge imaging). Volumes were obtained at a rate of 11.4 Hz and 8.2 Hz, respectively. The ball position was tracked at 200 Hz and synchronized to the calcium imaging using TTL pulses triggered after each frame grab.

For the single ring neuron FLP-out experiments, high resolution stacks were taken at the end of every experimental session to inspect the ring anatomy. These stacks were 1024 × 1024 pixels, with 25 planes each spaced 2 μm apart, and the laser power was turned up to ~100 mW to obtain 20 volumes with these parameters.

Open and closed-loop visual display—A custom-built digital micromirror device (DMD) projector system was used to show visual stimuli to the flies. A 240°, 2.5 inch tall, 3 inch diameter, cylindrical frame was 3D printed and covered with a single white diffuser sheet (V-HHDE-PM06-S01-D01 sample, BrightView Technologies, Durham, NC, USA). Three projectors each covered 80° of the screen (two DepthQ WXGA 360 HD 3D Projector, developed by Anthony Leonardo, Janelia, and Lightspeed Design, Bellevue, WA, USA and one Texas Instruments DLP 3010 Light Control). These projectors were modified to accommodate external blue LEDs as their light source (ThorLabs M455L3 455 nm LEDs with two Semrock BrightLine 447/60 nm bandpass filters in the path)

Custom C++ code using the OpenGL API generated the visual projections, which was either a completely dark virtual arena or a 15° bright stripe on a dark background. The projections were rendered with an Nvidia Quaddro K4000 graphics card. The code creates virtual objects and then uses the treadmill positional data to update the objects' positions as the fly moves. Brightness and spatial distortions due to the cylindrical screen are corrected via the software.

The voltage from a photodiode placed on top of the screen was recorded with a DAQ each time the projection was updated (at a 360 Hz framerate). The DAQ also recorded a TTL pulse each time a calcium imaging frame was grabbed. The two signals were then registered with respect to one another to link activity and behavior.

Visual stimuli consisted of one of four different conditions: darkness, a closed-loop stripe, an open loop stripe that circled the projection screen every 5 s, or a closed-loop stripe that periodically underwent open-loop jumps of 120°. For the closed-loop stripe trials, whenever the stripe moved into the 120° arc behind the fly where no screen or projector was present, it was moved such that it immediately appeared on the other side, making the closed-loop span effectively 240°.

Shi experiments—Experiments using the temperature sensitive, synaptic vesicle reuptake inhibitor Shibire^{ts} were performed as described in (Turner-Evans et al., 2017). Briefly, the first two trials occurred at room temperature (the permissive temperature). Heated saline was then perfused across the brain until a temperature of 30°C (the restrictive temperature) was reached, as measured by a thermocouple placed near the head capsule. The fly was then shown a closed-loop 15° stripe for 10 min, during which time the temperature was stabilized at 30°C. Three trials were then performed at the elevated temperature.

Kir experiments—At low temperatures, Gal80ts inhibits Gal4 transcriptional activity. At high temperatures, Gal80ts becomes inactive, leading to kir transcription. Flies were reared and raised for one day at 21.5°C before being split into two groups. Group one (the control group) was maintained at 21.5°C for two more days while group two (the experimental group) was shifted to a 30°C incubator. At 30°C, Gal80ts becomes inactive, allowing kir to be transcribed. Immediately before each experiment, either control or experimental flies were taken out of the incubator and dissected and measured at room temperature.

Electron microscopy reconstruction: Neuron Tracing—Neuron reconstructions were created from manual skeleton tracing of neuronal arbors and annotation of synapses from image stacks in CATMAID (http://www.catmaid.org) as described in Zheng et al. (2018). In brief, all neurons included in analyses were reconstructed by a minimum of two team members, an initial tracer and a subsequent proofreader who corroborated the tracer's work. To parallelize reconstruction efforts, some neurons were assigned more than one initial tracer and/or more than one proofreader. If a tracer or proofreader encountered ambiguous features (neural processes or synapses that were not identifiable with high confidence), (s)he consulted other tracers and proofreaders to determine the validity of the features in question, enlisting more expert tracers as needed. Any feature that remained ambiguous after scrutiny by an expert tracer was not included in the neural reconstruction and/or flagged to be excluded from analyses. During the proofreading phase, the proofreaders and tracers iteratively consulted each other until each neuron was deemed morphologically and synaptically correct per its tracing objective. Chemical synapse identification required that at least three of the following features were present, with the first being required: 1) an active zone including vesicles; 2) presynaptic specializations (i.e. a ribbon or T-bar with or without a platform); 3) synaptic clefts; 4) postsynaptic membrane specializations such as postsynaptic densities (PSDs). In cases where PSDs were not visible, all cells with membranes that had unobstructed access to a clearly visible synaptic cleft were annotated as postsynaptic. Since gap junctions are unlikely to be resolved at the resolution of this dataset we made no effort to annotate them.

Electron microscopy reconstruction: Tracing to classification—Neural reconstruction of microtubule-containing backbone neurites (see Schneider-Mizell et al., 2016) or gross morphology alone is often sufficient to classify a neuron based on expert identification or searching of existing LM datasets with NBLAST software (Costa et al., 2016). Neurons traced to classification were at a minimum reconstructed, with or without synapses, to the point at which their gross morphologies (i.e. backbone skeletons) unambiguously matched that observed by LM for a given cell class, or were unambiguously deemed to be a new cell type not previously observed.

Electron microscopy reconstruction: Tracing to completion—Every identifiable neurite was traced to achieve morphological completion, and every identifiable presynaptic release site or postsynaptic density was annotated to achieve pre- or postsynaptic completion, respectively, for a given neuron. Some neurons were traced to morphological or synaptic completion only on portions of their arbors or only in certain brain regions (e.g., D7 presynaptic glomeruli were traced to morphological and synaptic completion, whereas the remainder of these neurons were only traced to classification).

RNA Sequencing: Overview—Three different types of sequencing protocols were performed: bulk sequencing for the EPGs, Δ7s, PEN2s, and PEGs, low-cell sequencing for the PEN2s and R4m neurons, and single cell sequencing for the PEN1 and PEN2 lines. The low-cell sequencing protocol, which was developed after an initial round of bulk sequencing, allowed for more replicates and therefore was used at a later point to obtain R4d expression data. The PEN1 and PEN2 cell lines each have an additional cell type (PFN neurons for each) and therefore single cell sequencing was performed on these lines to look for different expression patterns across cells. We were unable to convincingly cluster the single cell results into two or more groups (data not shown) and therefore the mean expression was considered across the single cell replicates.

RNA Sequencing: Expression checks—Neurons of interest were isolated by expressing the fluorescent reporter 10XUAS-IVS-myr::GFP; 10XUAS-IVS-nls-tdTomato using split-Gal4 drivers specific for particular cell types and then manually picking the fluorescent neurons from dissociated brain tissue. As a preliminary to the sorting process, each driver/reporter combination was 'expression checked' to determine if the marked cells were sufficiently bright to be sorted effectively and if there was any off-target expression in neurons other than those of interest. Drivers that met both these requirements were used in sorting experiments as described below.

RNA Sequencing: Sorting of fluorescent-labelled neurons—*Drosophila* adults were collected daily as they eclosed, and aged 3–5 days prior to dissection. For each sample, 60–100 brains were dissected in freshly prepared, ice cold Adult Hemolymph Solution (AHS, 108 mM NaCl, 5 mM KCl, 2 mM $CaCl_2$, 8.2 mM $MgCl_2$, 4 mM $NaHCO_3$, 1 mM NH_2PO_4, 5 mM HEPES, 6 mM Trehalose, 10 mM Sucrose), and the major tracheal branches removed. The brains were transferred to a 1.5 ml Eppendorf tube containing 500 μl 1 mg/ml Liberase DH (Roche, prepared according to the manufacturer's recommendation) in AHS, and digested for 1 h at room temperature. The Liberase solution was removed and the brains washed twice with 800 microliters ice cold AHS. The final wash was removed completely and 400 μl of AHS+2% Fetal Bovine Serum (FBS, Sigma) were added. The brain samples were gently triturated with a series of fire-polished, FBS-coated Pasteur pipettes of descending pore sizes until the tissue was homogenized, after which the tube was allowed to stand for 2–3 m so that the larger debris could settle.

For hand sorting, the cell suspension was transferred to a Sylgard-lined Glass Bottom Dish (Willco Wells), leaving the debris at the bottom of the Eppendorf tube, and distributed evenly in a rectangular area in the center of the plate with the pipet tip. The cells were allowed to settle for 10–30 m prior to picking. Fluorescent cells were picked with a mouth aspirator consisting of a 0.8 mm Nalgene Syringe Filter (Thermo), a short stretch of tubing, a plastic needle holder, and a pulled Kwik-Fil Borosilicate Glass capillary (Fisher). Cells picked off the primary plate were transferred to a Sylgard-lined 35 mm Mat Tek Glass Bottom Microwell Dishes (Mat Tek) filled with 170 μl AHS+2%FBS, allowed to settle, and then re-picked. Three washes were performed in this way before the purified cells were picked and transferred into 50 μl buffer XB from the PicoPure RNA Isolation Kit (Life Technologies), lysed for 5 m at 42°C, and stored at −80°C.

For FACS, the samples were triturated in AHS+2%FBS that was run through a 0.2 μm filter, and the cell suspension was passed through a Falcon 5 ml round-bottom tube fitted with a 35 μm cell strainer cap (Fisher). Samples were sorted on a SONY SH800 cell sorter gated for single cells with a fluorescence intensity exceeding that of a non-fluorescent control. For bulk samples, GFP+tdTom+ events were purity sorted directly into 50 microliters PicoPure XB buffer, the sample lysed for 5 m at 42°C, and stored at −80°C. For low-cell samples, replicates of 40 cells were either purity sorted directly or yield sorted to enrich for GFP+tdTom+ cells followed by a purity sort into 3 μL Lysis Buffer (0.2% Triton X-100, 0.1 U/μL RNAsin) and flash frozen on dry ice. For single-cell (scRNA-Seq), individual cells were purity sorted directly into a 96-well plate containing 3 μL Lysis Buffer per well.

RNA Sequencing: Library preparation and sequencing—For bulk samples, total RNA was extracted from 100–500 pooled cells using the PicoPure kit (Life Technologies) according to the manufacturer's recommendation, including the on-column DNAse1 step. The extracted RNA was converted to cDNA and amplified with the Ovation RNA-Seq System V2 (NuGEN), and the yield quantified by NanoDrop (Thermo). The cDNA was fragmented and the sequencing adaptors ligated onto the fragments using the Ovation Rapid Library System (NuGEN). Library quality and concentration was determined with the Kapa Illumina Library Quantification Kit (KK4854, Kapa Biosystems), and the libraries were pooled and sequenced on an Illumina NextSeq 550 with 75 base pair reads. Sequencing adapters were trimmed from the reads with Cutadapt (Martin, 2011) prior to alignment with STAR (Dobin et al., 2013) to the *Drosophila* r6.17 genome assembly (Flybase). The resulting transcript alignments were passed to RSEM (Li and Dewey, 2011) to generate gene expression counts.

For low-cell and single-cell samples, one microliter of harsh lysis buffer (50 mM Tris pH 8.0, 5 mM EDTA pH 8.0, 10 mM DTT, 1% Tween-20, 1% Triton X-100, 0.1 g/L Proteinase K (Roche), 2.5 mM dNTPs (Takara), and ERCC Mix 1 (Thermo-Fisher) diluted to 1e-7) and 1 μl10 μM barcoded RT primer were added, and the samples were incubated for 5 m at 50°C to lyse the cells, followed by 20 m at 80°C to inactivate the Proteinase K. Reverse transcription master mix (2 μL 5X RT Buffer (Thermo-Fisher), 2 μL 5M Betaine (Sigma-Aldrich), 0.2 μL 50 μM E5V6NEXT template-switch oligo (Integrated DNA Technologies), 0.1 μL 200 U/μL Maxima H-RT (Thermo-Fisher), 0.1 μL 40U/μL RNAsin (Lucigen), and 0.6 μL nuclease-free water (Thermo-Fisher) was added to the lysis reaction and incubated at 42°C for 1.5 h, followed by 10 m at 75°C to inactivate the reverse transcriptase. PCR was performed by adding 10 μL 2X HiFi PCR Mix (Kapa Biosystems) and 0.5 μL 60 μM SINGV6 primer and incubating at 98°C for 3 m, followed by 20 cycles of 98°C for 20 s, 64°C for 15 s, 72°C for 4 m, and a final extension of 5 m at 72°C. Groups of 8 reactions were pooled to yield ~250 μL and purified with Ampure XP Beads (0.6x ratio; Beckman Coulter), washed twice with 75% Ethanol, and eluted in 40 μL nuclease-free water. The DNA concentration of each sample was determined using Qubit High-Sensitivity DNA kit (Thermo-Fisher).

To prepare the Illumina sequencing library, 600 pg cDNA from each pooled sample was used in a modified Nextera XT library preparation (Illumina) (Soumillon et al., 2014) using the P5NEXTPT5 primer and extending the tagmentation time to 15 m. The resulting libraries were purified according to the Nextera XT protocol (0.6x ratio) and quantified by qPCR using Kapa Library Quantification (Kapa Biosystems). Six to eight sequencing libraries were loaded on a NextSeq High Output flow cell reading 26 bases in Read 1, including the spacer, sample barcode and UMI, 8 bases in the i7 index read, and 50 bases in Read 2 representing the cDNA fragment from the 3' end of the transcript.

For post-sequencing processing, sample barcode and UMI sequences were extracted from Read 1 using custom python scripts. Barcode error correction was done using starcode v1.1 (Zorita et al., 2015) with the following additional parameters: “-d l -q --print_clusters”. Read 2 sequences were renamed using the error-corrected barcode from the starcode and UMI sequences from Read 1, and were aligned to the *Drosophila melanogaster* genome assembly r6.17 from Flybase (flybase.org) using STAR (Dobin et al., 2013) with the following additional parameters: “— alignIntronMax 200000 --outSAMattributes All --outSAMunmapped Within --out SAMtype BAM Unsorted”. An alignment is considered valid if it aligns to an exon feature on the correct strand and is unique. Valid alignments that had at least 50% of the read aligned to an exon feature were used to create gene-level counts using a custom python script to collapse UMIs by gene. All custom scripts available upon request.

Fluoresence *in Situ* Hybridization—Fluorescence in situ hybridization followed the protocol outlined in (Meissner et al., 2019)

Stochastic expression of GCaMP6f in ring neurons with the FLP-out technique—Flies were reared at 25°C. Less than one day after eclosion, adults were heat shocked in a water bath at 37°C for 8 min, which consistently lead to 0–3 individual neurons labeled with GCaMP.

Simulation

Biophysical modelling of P-EN2s—All biophysical modelling was done using NEURON with python software (Hines et al., 2009). For the simulations, neurons of interest were first imported into python using pymaid (https://pymaid.readthedocs.io). They were then simplified by removing all stretches of nodes that were not branchpoints or synapses and replacing them with a single straight cylinder of the same length. The width of the cylinder was taken to be $d = 0.442\ \mu m$ for axonic regions and $d = (0.442 - 0.025)e^{-0.040589\ l} + 0.025$ for dendritic regions, where d is given in μm and l is measured in nm. These values were based on empirical data from the EM images. For all simulations, we set $E_{rest} = -55\ mV$, $R_m = 20800\ \Omega cm^2$, $C_m = 0.79\ uF\ cm^{-2}$, and $R_a = 266\ \Omega cm$ (Gouwens and Wilson, 2009). We implemented all synapses as NEURON Exp2Syn synapses and let cholinergic synapses have a reversal potential of $E_{rev} = 0\ mV$, time constants of $\tau_1 = 0.61\ ms$ and $\tau_2 = 2.11\ ms$, and a maximum conductance of $16/75000\ \mu S$ (Lee and O’Dowd, 1999).

To quantify the variability in potential within and between neuropils in P-EN2 neurons for a given number of input synapses n, we first selected n Δ7 input synapses at random 10 times in each of the 5 P-EN2 neurons for which we have traced Δ7 input neurons. We then ran a NEURON simulation for 70 ms with each input synapse firing thrice at 25 ms intervals with a NetStim noise parameter of 0.2. In the EB, we quantified the potential at all E-PG output synapses and found the maximum potential for each synapse. We then averaged the mean and standard deviation of these maximum potentials across all simulations for a given n. In the PB we averaged the maximum potentials over all input synapses from Δ7 neurons since the P-EN2 neurons do not have significant output in the PB.

Extrapolation of the ring attractor weight matrix from Turner-Evans*, Wegener*, et al.

Extrapolation of the ring attractor weight matrix from Turner-Evans*, Wegener*, et al.—The rate model in (Turner-Evans et al., 2017) only explicitly included the E-PGs and P-EN1s. Inhibition was implicitly assumed to come from the Δ7s, but it was incorporated into the E-PG connectivity matrix. Each E-PG was assumed to inhibit all P-EN1s equally, but for the P-EN1s which shared a given E-PG's heading tuning: these were inhibited more weakly.

For Figure 8A, the Δ7s were instead assumed to act as a standalone population. In this scenario, each Δ7 inhibits one P-EN1 and receives excitatory input from all E-PGs except for the one that shares the chosen P-ENl's heading tuning. In the limit that the Δ7 time constant goes to 0, the weight matrix in Figure 8A will match that of (Turner-Evans et al., 2017).

Data Analysis

Calcium imaging and behavior preprocessing—Maximum intensity projections were obtained for each volume within a stack. To correct for movement, a mean of the individual projections was then computed, and each projection was registered to the mean through normalized cross correlation. In the case of two-color imaging, the green channel was used for registration.

Reference regions of interest were defined for each fly by drawing polygons over the mean maximum intensity projection of a chosen stack. For two-color imaging a composite of the two channels was used. For protocerebral bridge imaging, eighteen polygons were placed over the structure, one for each glomerulus. For ellipsoid body imaging, ellipses were drawn over the inner and outer circumference of the structure and the inner region equi-angularly divided into 16 regions.

The registered stacks were then Gaussian filtered with a 2×2 pixel size and a standard deviation of 0.5 pixels. The normalized change in fluorescence for each region was calculated as follows. The baseline fluorescence was taken as the mean of the lowest 10% fluorescence values over the experiment. All fluorescence values were then normalized by this value and then 1 was subtracted from them.

The recorded behavioral data was registered to the imaging stacks through the frame grab and photodiode signals (see third paragraph of open and closed-loop visual display above).

Population vector average (PVA)—The MATLAB-based Circular Statistics Toolbox (Berens, 2009) was used to calculate the population vector average (PVA) and the population vector average strength. The PVA is the circular mean (circ_mean) of the 16 ROIs while the PVA strength is their resultant vector length (circ_r).

Unwrapping heading and PVA signals—The heading and PVA signals were unwrapped by finding time points where the signal jumped by more than π or $2\pi/3$, respectively. The signal was then shifted up or down by 2π at those points, as appropriate.

Quantifying bump stability—We quantified the bump's stability as follows. First, we plotted how much the bump's angular orientation changed versus how much the fly's heading direction changed at every time point in a 5 s sliding window (see Figure S1C–E). To pick the time window for this analysis, we first plotted the median correlation between bump position and fly orientation within different time windows. We picked the time window for which the correlation values began to saturate for all the conditions that we analyzed (darkness and closed-loop; permissive and restrictive temperatures in control and Shi flies), but during which time the bump could still be tracked (for some Shi experiments, the bump became difficult to track for longer intervals at the restrictive temperature). We then fit a line to these points and calculated the slope. The slope was the gain between the fly's turns and the bump's movements. A gain of 1 implied that the bump perfectly tracked the fly's heading direction.

AOTU Shi knockout analysis: Calcium activity and behavior—The offset between the bump position and the fly's heading was calculated by taking the difference between the PVA and the heading. This offset was then binned into 17 linearly spaced bins between $-\pi$ and π. The mean resultant vector length was calculated using the circ_r function described above. The behavior was binned and analyzed in the same way, though now the stripe position was used.

Electron microscopy skeleton rendering—Traced neurons were imported into Blender using Philipp Schlegel's CATMAID-to-Blender plugin (https://github.com/schlegelp/CATMAID-to-Blender) (Schlegel et al., 2016). Classes were then separated into layers; their synaptic inputs and outputs were removed; and they were given unique colors. The bevel depth (spline thickness) was increased and shaded using a Strahler analysis (alpha decreases as branch order increases away from root node). Finally, cameras were snapped to the neuron bounding dimensions, a hemi lamp was added, and the resulting images were rendered as 200% resolution png files.

Connectivity matrices and distributions—Analyses were carried out in python after importing the neurons using pymaid. For all neuropil-specific analyses, neurons were divided into distinct regions at points along the axon approximately halfway between each pair of neuropils. Connectivity matrices were generated in python using pyplot's imshow function and the 'Reds' colormap.

In the following, we use uppercase letters (A, B) to refer to types of neurons, and lowercase letters (a, b) to refer to single neurons of type A/B. The fraction of input synapses to a neuron a that come from a given type of neurons B was calculated as the number of annotated synapses from B to a divided by the total number of annotated postsynaptic sites on a. The fraction of output synapses from a to B was calculated similarly.

Estimates of total connectivity distributions—Estimates of the total proportion of connectivity accounted for by the cell types considered in the present manuscript were based on light-level anatomy from Wolff et al. (2015). We assume that the central complex contains 16 P-EN1, P-EN2, and P-EG neurons, 54 E-PG neurons, 40 Δ7 neurons, and 100 ring neurons.

In the noduli, we assume that there is no compartmentalization and that neurons are distributed evenly between the left and right noduli. We treat the left and right noduli separately. We thus take the estimated connectivity from a neuron *a* to a neuron *b* in a nodulus to be the mean fraction of output synapses from a neuron *a*' that go to a neuron *b*', averaged over all pairs of *A* and *B* neurons, times the total number of presynaptic sites in neuron *a*. To estimate the number of post-synapses in *b* that come from *a*, we take the mean number of synapses in *b*' that come from *a*', averaged over all pairs, and multiply by the total input to *b*. For the total output from neuron *a* to any neuron of type *B*, we multiply the connectivity from neuron *a* to neuron *b* by the total number of neurons of type *B* in a nodulus. For the compartmentalized neuropils discussed below, we instead multiply the compartment-specific average connectivity by the total number of neurons of the relevant type in the compartment.

In the PB, we assume that connections between P-EN, E-PG and P-EG neurons only occur within a single glomerulus. We take the average connectivity between each pair of these types of neurons to be the average over all glomeruli for which we have data, assuming 1 P-EN/P-EG neuron, 3 E-PG neurons, and 5 Δ7 neurons per glomerulus when calculating total connectivity. We assume that each Δ7 neuron gives output to two glomeruli where it does not receive any input and that the Δ7 input is uniformly distributed across the remaining glomeruli. This violates the known anatomy of the Δ7 neurons but provides a good approximation to average and total connectivities given the limited number of glomeruli from which we have data. When estimating Δ7-Δ7 connectivity, we do not consider any compartmentalization.

In the EB, we estimate connectivities to and from E-PG neurons at the level of wedges and connectivities between P-EG and P-EN neurons at the level of tiles. Each tile covers 45° of the EB. For tile neurons, we consider the total connectivity to be the sum of the total connectivity within the same tile and the connectivity to and from the two neighboring tiles. For E-PG neurons, we similarly consider connectivity within the same wedge and to the two neighboring wedges in the case of connectivity with wedge neurons, and tiles in the case of connectivity with tile neurons. For a given pair of neuron types and compartment or pair of compartments, connectivity is estimated as described for the noduli above. We assume ring neurons to be uniformly distributed throughout the EB and do not distinguish between different classes of ring neurons.

FIBSEM connectivity matrices and comparison to FAFB data—Connectivity data for the FIBSEM dataset was accessed using the neuprintr API (https://github.com/natverse/neuprintr) (Bates et al., 2019). The ROIweight parameter (a count of the postsynaptic densities in a given ROI) was used to define the synapse counts in all FIBSEM connectivity matrices. Note that the FAFB labels for PB glomeruli are flipped relative to those for the FIBSEM connectome (for example, glomerulus R6 in the FAFB dataset would be glomerulus L6 in the FIBSEM dataset), so all FIBSEM neurons were manually relabeled (L and R were switched) for all figures and analyses to make the comparisons more relevant.

The FIBSEM dataset contains three E-PG neurons in L6 and R6 (whereas only two were identified and traced in the FAFB dataset), five each of the 5R4L, 6R3L, 2R7L, and 1R9R8L

Δ7 neurons (whereas two, two, one, and one of each, respectively were traced in the FAFB dataset), and three of the 7R2L Δ7 neurons (one was traced in the FAFB dataset). To directly compare connectivity across datasets, a random subset of 6R/6L E-PGs and Δ7s were chosen from the FIBSEM dataset to match the number of neurons in the FAFB dataset. For all other neurons (P-EN1s, P-EN2s, P-EGs, and 5R/5L E-PGs), the numbers in the FIBSEM and FAFB dataset were equivalent, so all neurons were selected. Connections between partners across datasets were then compared using two metrics. First, all instances where one dataset had connections that were absent in the other were noted. Second, where both datasets showed connections between neurons, the synapse counts were compared by calculating the normalized difference between counts across the two datasets: (# of FAFB synapses - # of FIBSEM synapses) / (# of FAFB synapses + # of FIBSEM synapses). In the NO, there are two P-EN1s and two P-EN2s each in glomeruli 6L and 6R. Thus, there are a total of $2^4 = 16$ possible permutations of the FIBSEM data that can be compared to the FAFB data. Each of these was considered to generate the violin plots shown in Figure S13E and S13F. In the EB and PB, the number of possible permutations is much larger (622,080,000 for the PB and 20,736 for the EB). For these ROIS, 200 possible combinations were considered. For these combinations, for which there were more FIBSEM neurons than FAFB neurons, a subset of the FIBSEM neurons was randomly selected, and then, whenever there was more than one neuron that arborized within a given glomerulus, the FIBSEM neurons were randomly shuffled to compare to the FAFB data.

RNA Seq analysis, plotting—Reads were aligned to the Drosophila genome and transcriptome annotation using FlyBase (Thurmond et al., 2019). For each sample, raw read counts were normalized by the total number of reads per million mapped reads per sample to yield counts per million (CPM) measurements. $\mathrm{Log}_{10}(\mathrm{CPM}+1)$ values for the expression of different gene sets (receptors, neurotransmitters, etc.) were plotted as heatmaps using the pcolor function in matplotlib.pyplot using the default viridis color plate. For the statistical analysis of differential gene expression, the edgeR package (Robinson et al., 2010) in R was used on the raw count data, with the standard workflow; this consists of estimating the negative binomial fit of the mean-dispersion relationship through a weighted-likelihood empirical Bayesian approach (estimateDisp function), and then calculating p-values through a gene-wise negative binomal generalized linear model with quasi-likelihood tests (glmQLFit function).

E-PGs: Shi experiments—The PVA strength was calculated as outlined in the Population Vector Average (PVA) section, and the mean of PVA strength was then computed across the entire trial.

Δ7s and E-PGs: Two color calcium imaging analysis—For the registered bump activity plots shown in Figure 4I, the maximum of the red channel was found at each time point, and the activity profiles of the red and green time channels across ROIs were each circularly shifted by the same number of glomeruli so that red channel peak was positioned at glomerulus 4. These profiles were then sorted by rotational velocity, across 7 bins between $-\pi$ and π rad/s. The mean PVA was then found for these sorted profiles, and the difference between them calculated and plotted in Figure 4J.

Δ7s and E-PGs: Shi experiments—A 5 s sliding window was moved over the PVA and heading data. If the PVA strength was over 0.075 within that window (meaning that a clear bump of activity was present), the PVA was plotted with respect to the heading, and the slope and correlation coefficient were calculated. These slopes were then placed into one of 21 linearly spaced bins between −4 and 4. The median slope and the 25th to 75th percentile range were then calculated.

Fluorescence *in Situ* Hybridization data analysis—63x images were manually inspected for overlap between the GFP tagged cell bodies and the tagged neurotransmitter specific mRNA.

FLP-out ring neuron analysis—Five trials were run for each fly. The activity was then averaged over these trials. Open-loop responses were further averaged over all six clockwise or counterclockwise repetitions. The maximum or minimum activity was then found for these averaged signals.

Population ring neuron analysis—Regions of interest were manually drawn over the center ring and around between 2 to 4 visible glomeruli on each side in the BU. The signal in these ROIs was then averaged over the 5 trials.

P-EN2s and P-EGs: Two-color calcium imaging analysis—The PVA was calculated for both the P-EN2s and the P-EGs. Time points were then binned by rotational velocity (in one of eight equally spaced bins between $-\pi$ and π rad/s). At times when the PVA strength was greater than 0.1, the difference between the P-EG and the P-EN2 PVA was calculated and the mean and standard deviation calculated over all points within a given bin. The full-width-at-half-maximum (FWHM) of the activity was similarly calculated at each point in time and binned by rotational velocity. The mean FWHM for each bin was then calculated. The mean and SD of the PVA difference in each bin was then divided by the corresponding mean FWHM to arrive at the plot in Figure 7H. For the plot in Figure 7I, each individual PVA difference was divided by the FWHM that fell within its rotational velocity bin and all of these width normalized values were then averaged.

Cross-correlation between the maximum red or green ΔF/F and the rotational or forward velocity was calculated using the corrcoef function in MATLAB (MathWorks Inc., Natick MA) for each time lag (Figure S9A–D).

P-EN2s and P-EGs: Kir experiments—The PVA strength of the signal was calculated at each time point and binned according to the rotational speed (in one of 11 equally space bins between 0 and π). The mean and standard deviation were then calculated over all points within a given bin.

The mean ΔF/F for the off-peak ROIs was calculated as follows: the maximum ΔF/F ROI was found, and that ROI and one on either side of it were excluded from the analysis. The mean of the remaining 13 ROIs was then found and binned and analyzed as above for the PVA Strength (Figure S9J, S9K)

P-EN2 and E-PG: EB projections—The signals were registered to the red, E-PG peak and sorted by rotational velocity as outlined in the "Δ7s and E-PGs: Two color calcium imaging analysis" section.

Supplementary Material

Refer to Web version on PubMed Central for supplementary material.

Acknowledgments

We thank Ruchi Parekh and many members of Janelia's CAT for help with reconstructing neurons, in particular: Marisa Dreher, Chris Patrick, Tansy Yang, Cullen Moran, John Walsh, Neha, Kelli Fairbanks, Mia Ndama and Maggie Greer. We also thank Marisa Dreher for renders of Δ7 neurons from the FIBSEM dataset. We are also grateful to interns, Claire Peterson, Stanley Tran and Boyd Qu for neuron tracing. We thank the Janelia Quantitative Genomics team for performing RNA sequencing and Vilas Menon for helpful advice on RNA-Seq data analysis, and Geoffrey Meissner for carrying out the FISH experiments. We are grateful to Romain Franconville for his help in selecting Gal4 lines suitable for FISH and RNA-Seq, to Ed Rogers, Karen Hibbard, and Michael Rogers for generously providing fly constructs, and also for advice on fly wrangling. We thank Scarlett Harrison, Guillermo Gonzolez, Brenda Paez and Todd Laverty for help with fly husbandry; Vasily Goncharov, Chris McRaven, and Jon Arnold for assistance with the two-photon microscope; Bill Biddle for hardware assistance for the VR setup; and Jim Strother for initial code for the VR setup. We thank Brad Hulse for initial code and discussion on bump stability analyses; Hannah Haberkern for insights on behavior. Finally, we thank Sung Soo Kim, Chuntao Dan, Ann Hermundstad, Romain Franconville, Brad Hulse, and Hannah Haberkern for all around good advice and feedback.

References

Amari S (1977). Dynamics of pattern formation in lateral-inhibition type neural fields. Biol Cybern 27, 77–87. [PubMed: 911931]

Aso Y, Ray RP, Long X, Bushey D, Cichewicz K, Ngo TT, Sharp B, Christoforou C, Hu A, Lemire AL, et al. (2019). Nitric oxide acts as a cotransmitter in a subset of dopaminergic neurons to diversify memory dynamics. Elife 8.

Bahl A, Ammer G, Schilling T, and Borst A (2013). Object tracking in motion-blind flies. Nat Neurosci 16, 730–738. [PubMed: 23624513]

Bates AS, Manton JD, Jagannathan SR, Costa M, Schlegel P, Rohlfing T, and Jefferis GSXE (2019). The natverse: a versatile computational toolbox to combine and analyse neuroanatomical data. bioRxiv, 006353.

Ben-Yishai R, Bar-Or RL, and Sompolinsky H (1995). Theory of orientation tuning in visual cortex. Proc Natl Acad Sci U S A 92, 3844–3848. [PubMed: 7731993]

Bender JA, Pollack AJ, and Ritzmann RE (2010). Neural activity in the central complex of the insect brain is linked to locomotor changes. Curr Biol 20, 921–926. [PubMed: 20451382]

Berens P (2009). CircStat: A MATLAB toolbox for circular statistics. J Stat Softw 31, 1–21.

Burak Y, and Fiete IR (2012). Fundamental limits on persistent activity in networks of noisy neurons. Proc Natl Acad Sci U S A 109, 17645–17650. [PubMed: 23047704]

Butler WN, Smith KS, van der Meer MAA, and Taube JS (2017). The Head-Direction Signal Plays a Functional Role as a Neural Compass during Navigation. Curr Biol 27, 1259–1267. [PubMed: 28416119]

Chaudhuri R, Gercek B, Pandey B, Peyrache A, and Fiete I (2019). The population dynamics of a canonical cognitive circuit. 516021.

Chen TW, Wardill TJ, Sun Y, Pulver SR, Renninger SL, Baohan A, Schreiter ER, Kerr RA, Orger MB, Jayaraman V, et al. (2013). Ultrasensitive fluorescent proteins for imaging neuronal activity. Nature 499, 295–300. [PubMed: 23868258]

Clark BJ, and Taube JS (2012). Vestibular and attractor network basis of the head direction cell signal in subcortical circuits. Front Neural Circuit 6.

Compte A, Brunel N, Goldman-Rakic PS, and Wang XJ (2000). Synaptic mechanisms and network dynamics underlying spatial working memory in a cortical network model. Cereb Cortex 10, 910–923. [PubMed: 10982751]

Cope AJ, Sabo C, Vasilaki E, Barron AB, and Marshall JA (2017). A computational model of the integration of landmarks and motion in the insect central complex. PLoS One 12, e0172325. [PubMed: 28241061]

Daniels RW, Gelfand MV, Collins CA, and DiAntonio A (2008). Visualizing glutamatergic cell bodies and synapses in Drosophila larval and adult CNS. J Comp Neurol 508, 131–152. [PubMed: 18302156]

Davis FP, Nern A, Picard S, Reiser MB, Rubin GM, Eddy SR, and Henry GL (2019). A genetic, genomic, and computational resource for exploring neural circuit function. bioRxiv, 385476.

Dobin A, Davis CA, Schlesinger F, Drenkow J, Zaleski C, Jha S, Batut P, Chaisson M, and Gingeras TR (2013). STAR: ultrafast universal RNA-seq aligner. Bioinformatics 29, 15–21. [PubMed: 23104886]

Donlea JM, Pimentel D, Talbot CB, Kempf A, Omoto JJ, Hartenstein V, and Miesenbock G (2018). Recurrent Circuitry for Balancing Sleep Need and Sleep. Neuron 97, 378–389 e374. [PubMed: 29307711]

Dus M, Ai M, and Suh GS (2013). Taste-independent nutrient selection is mediated by a brain-specific Na+ /solute co-transporter in Drosophila. Nat Neurosci 16, 526–528. [PubMed: 23542692]

el Jundi B, Pfeiffer K, Heinze S, and Homberg U (2014). Integration of polarization and chromatic cues in the insect sky compass. J Comp Physiol A Neuroethol Sens Neural Behav Physiol 200, 575–589. [PubMed: 24589854]

el Jundi B, Warrant EJ, Byrne MJ, Khaldy L, Baird E, Smolka J, and Dacke M (2015). Neural coding underlying the cue preference for celestial orientation. Proc Natl Acad Sci U S A 112, 11395–11400. [PubMed: 26305929]

Enell L, Hamasaka Y, Kolodziejczyk A, and Nassel DR (2007). gamma-Aminobutyric acid (GABA) signaling components in Drosophila: immunocytochemical localization of GABA(B) receptors in relation to the GABA(A) receptor subunit RDL and a vesicular GABA transporter. J Comp Neurol 505, 18–31. [PubMed: 17729251]

Fisher YE, Lu J, D'Alessandro I, and Wilson RI (2019). Sensorimotor experience remaps visual input to a heading-direction network. Nature 576, 121–125. [PubMed: 31748749]

Franconville R, Beron C, and Jayaraman V (2018). Building a functional connectome of the Drosophila central complex. Elife 7.

Giraldo YM, Leitch KJ, Ros IG, Warren TL, Weir PT, and Dickinson MH (2018). Sun Navigation Requires Compass Neurons in Drosophila. Curr Biol 28, 2845–2852 e2844. [PubMed: 30174187]

Golic KG, and Lindquist S (1989). The FLP recombinase of yeast catalyzes site-specific recombination in the Drosophila genome. Cell 59, 499–509. [PubMed: 2509077]

Gouwens NW, and Wilson RI (2009). Signal propagation in Drosophila central neurons. J Neurosci 29, 6239–6249. [PubMed: 19439602]

Green J, Adachi A, Shah KK, Hirokawa JD, Magani PS, and Maimon G (2017). A neural circuit architecture for angular integration in Drosophila. Nature 546, 101–106. [PubMed: 28538731]

Green J, Vijayan V, Mussells Pires P, Adachi A, and Maimon G (2019). A neural heading estimate is compared with an internal goal to guide oriented navigation. Nat Neurosci 22, 1460–1468. [PubMed: 31332373]

Guo P, and Ritzmann RE (2013). Neural activity in the central complex of the cockroach brain is linked to turning behaviors. J Exp Biol 216, 992–1002. [PubMed: 23197098]

Han R, Huang H-P, Lee W-J, Chuang C-L, Yen H-H, Kao W-T, Chang H-Y, and Lo C-C (2019). Coordination between stabilizing circuits and updating circuits in spatial orientation working memory. bioRxiv, 819185.

Hanesch U, Fischbach KF, and Heisenberg M (1989). Neuronal architecture of the central complex in Drosophila-melanogaster. Cell Tissue Res 257, 343–366.

Hargreaves EL, Yoganarasimha D, and Knierim JJ (2007). Cohesiveness of spatial and directional representations recorded from neural ensembles in the anterior thalamus, parasubiculum, medial entorhinal cortex, and hippocampus. Hippocampus 17, 826–841. [PubMed: 17598156]

Heinze S, and Homberg U (2007). Maplike representation of celestial E-vector orientations in the brain of an insect. Science 315, 995–997. [PubMed: 17303756]

Heinze S, and Homberg U (2009). Linking the input to the output: New sets of neurons complement the polarization vision network in the locust central complex. Journal of Neuroscience 29, 4911–4921. [PubMed: 19369560]

Heinze S, and Reppert SM (2011). Sun compass integration of skylight cues in migratory monarch butterflies. Neuron 69, 345–358. [PubMed: 21262471]

Held M, Berz A, Hensgen R, Muenz TS, Scholl C, Rossler W, Homberg U, and Pfeiffer K (2016). Microglomerular Synaptic Complexes in the Sky-Compass Network of the Honeybee Connect Parallel Pathways from the Anterior Optic Tubercle to the Central Complex. Front Behav Neurosci 10, 186. [PubMed: 27774056]

Hines ML, Davison AP, and Muller E (2009). NEURON and Python. Front Neuroinform 3, 1. [PubMed: 19198661]

Homberg U, Heinze S, Pfeiffer K, Kinoshita M, and el Jundi B (2011). Central neural coding of sky polarization in insects. Philos Trans R Soc Lond B Biol Sci 366, 680–687. [PubMed: 21282171]

Homberg U, Hofer S, Pfeiffer K, and Gebhardt S (2003). Organization and neural connections of the anterior optic tubercle in the brain of the locust, Schistocerca gregaria. Journal of Comparative Neurology 462, 415–430.

Homberg U, Humberg TH, Seyfarth J, Bode K, and Perez MQ (2018). GABA immunostaining in the central complex of dicondylian insects. J Comp Neurol 526, 2301–2318. [PubMed: 30004590]

Homberg U, and Muller M (2016). Ultrastructure of GABA- and Tachykinin-Immunoreactive Neurons in the Lower Division of the Central Body of the Desert Locust. Front Behav Neurosci 10, 230. [PubMed: 27999533]

Homberg U, Vitzthum H, Muller M, and Binkle U (1999). Immunocytochemistry of GABA in the central complex of the locust Schistocerca gregaria: Identification of immunoreactive neurons and colocalization with neuropeptides. Journal of Comparative Neurology 409, 495–507.

Isaacman-Beck J, Paik KC, Wienecke CFR, Yang HH, Fisher YE, Wang IE, Ishida IG, Maimon G, Wilson RI, and Clandinin TR (2019). SPARC: a method to genetically manipulate precise proportions of cells. bioRxiv, 788679.

Itskov V, Hansel D, and Tsodyks M (2011). Short-Term Facilitation may Stabilize Parametric Working Memory Trace. Front Comput Neurosci 5, 40. [PubMed: 22028690]

Kahsai L, Carlsson MA, Winther AM, and Nassel DR (2012). Distribution of metabotropic receptors of serotonin, dopamine, GABA, glutamate, and short neuropeptide F in the central complex of Drosophila. Neuroscience 208, 11–26. [PubMed: 22361394]

Kakaria KS, and de Bivort BL (2017). Ring Attractor Dynamics Emerge from a Spiking Model of the Entire Protocerebral Bridge. Front Behav Neurosci 11, 8. [PubMed: 28261066]

Kim SS, Hermundstad AM, Romani S, Abbott LF, and Jayaraman V (2019). Generation of stable heading representations in diverse visual scenes. Nature 576, 126–131. [PubMed: 31748750]

Kim SS, Rouault H, Druckmann S, and Jayaraman V (2017). Ring attractor dynamics in the Drosophila central brain. Science 356, 849–853. [PubMed: 28473639]

Kitamoto T (2002). Conditional disruption of synaptic transmission induces male-male courtship behavior in Drosophila. Proc Natl Acad Sci U S A 99, 13232–13237. [PubMed: 12239352]

Knierim JJ, Kudrimoti HS, and McNaughton BL (1998). Interactions between idiothetic cues and external landmarks in the control of place cells and head direction cells. J Neurophysiol 80, 425–446. [PubMed: 9658061]

Knierim JJ, and Zhang KC (2012). Attractor dynamics of spatially correlated neural activity in the limbic system. Annual Review of Neuroscience, Vol 35 35, 267–285.

Krause T, Spindler L, Poeck B, and Strauss R (2019). Drosophila Acquires a Long-Lasting Body-Size Memory from Visual Feedback. Curr Biol 29, 1833–1841 e1833. [PubMed: 31104933]

Kunst M, Hughes ME, Raccuglia D, Felix M, Li M, Barnett G, Duah J, and Nitabach MN (2014). Calcitonin gene-related peptide neurons mediate sleep-specific circadian output in Drosophila. Curr Biol 24, 2652–2664. [PubMed: 25455031]

Kuntz S, Poeck B, and Strauss R (2017). Visual Working Memory Requires Permissive and Instructive NO/cGMP Signaling at Presynapses in the Drosophila Central Brain. Curr Biol 27, 613–623. [PubMed: 28216314]

Lee D, Huang TH, De La Cruz A, Callejas A, and Lois C (2017). Methods to investigate the structure and connectivity of the nervous system. Fly (Austin) 11, 224–238. [PubMed: 28277925]

Lee D, and O’Dowd DK (1999). Fast excitatory synaptic transmission mediated by nicotinic acetylcholine receptors in Drosophila neurons. J Neurosci 19, 5311–5321. [PubMed: 10377342]

Li B, and Dewey CN (2011). RSEM: accurate transcript quantification from RNA-Seq data with or without a reference genome. BMC Bioinformatics 12, 323. [PubMed: 21816040]

Liang X, Ho MCW, Zhang Y, Li Y, Wu MN, Holy TE, and Taghert PH (2019). Morning and Evening Circadian Pacemakers Independently Drive Premotor Centers via a Specific Dopamine Relay. Neuron 102, 843–857 e844. [PubMed: 30981533]

Lin CY, Chuang CC, Hua TE, Chen CC, Dickson BJ, Greenspan RJ, and Chiang AS (2013). A comprehensive wiring diagram of the protocerebral bridge for visual information processing in the Drosophila brain. Cell reports 3, 1739–1753. [PubMed: 23707064]

Liu G, Seiler H, Wen A, Zars T, Ito K, Wolf R, Heisenberg M, and Liu L (2006). Distinct memory traces for two visual features in the Drosophila brain. Nature 439, 551–556. [PubMed: 16452971]

Liu S, Liu Q, Tabuchi M, and Wu MN (2016). Sleep Drive Is Encoded by Neural Plastic Changes in a Dedicated Circuit. Cell 165, 1347–1360. [PubMed: 27212237]

Liu WW, and Wilson RI (2013). Glutamate is an inhibitory neurotransmitter in the Drosophila olfactory system. Proc Natl Acad Sci U S A 110, 10294–10299. [PubMed: 23729809]

Long X, Colonell J, Wong AM, Singer RH, and Lionnet T (2017). Quantitative mRNA imaging throughout the entire Drosophila brain. Nat Methods 14, 703–706. [PubMed: 28581495]

Martin M (2011). Cutadapt removes adapter sequences from high-throughput sequencing reads. 2011 17, 3.

Martin-Pena A, Acebes A, Rodriguez JR, Chevalier V, Casas-Tinto S, Triphan T, Strauss R, and Ferrus A (2014). Cell types and coincident synapses in the ellipsoid body of Drosophila. European Journal of Neuroscience 39, 1586–1601.

Meissner GW, Nern A, Singer RH, Wong AM, Malkesman O, and Long X (2019). Mapping Neurotransmitter Identity in the Whole-Mount Drosophila Brain Using Multiplex High-Throughput Fluorescence in Situ Hybridization. Genetics 211, 473–482. [PubMed: 30563859]

Muir GM, Brown JE, Carey JP, Hirvonen TP, Della Santina CC, Minor LB, and Taube JS (2009). Disruption of the Head Direction Cell Signal after Occlusion of the Semicircular Canals in the Freely Moving Chinchilla. Journal of Neuroscience 29, 14521–14533. [PubMed: 19923286]

Nern A, Pfeiffer BD, and Rubin GM (2015). Optimized tools for multicolor stochastic labeling reveal diverse stereotyped cell arrangements in the fly visual system. Proc Natl Acad Sci U S A 112, E2967–2976. [PubMed: 25964354]

Neuser K, Triphan T, Mronz M, Poeck B, and Strauss R (2008). Analysis of a spatial orientation memory in Drosophila. Nature 453, 1244–1247. [PubMed: 18509336]

Ocko SA, Hardcastle K, Giocomo LM, and Ganguli S (2018). Emergent elasticity in the neural code for space. Proceedings of the National Academy of Sciences.

Ofstad TA, Zuker CS, and Reiser MB (2011). Visual place learning in Drosophila melanogaster. Nature 474, 204–207. [PubMed: 21654803]

Omoto JJ, Keles MF, Nguyen BM, Bolanos C, Lovick JK, Frye MA, and Hartenstein V (2017). Visual Input to the Drosophila Central Complex by Developmentally and Functionally Distinct Neuronal Populations. Curr Biol 27, 1098–1110. [PubMed: 28366740]

Omoto JJ, Nguyen BM, Kandimalla P, Lovick JK, Donlea JM, and Hartenstein V (2018). Neuronal Constituents and Putative Interactions Within the Drosophila Ellipsoid Body Neuropil. Front Neural Circuits 12, 103. [PubMed: 30546298]

Page HJI, and Jeffery KJ (2018). Landmark-Based Updating of the Head Direction System by Retrosplenial Cortex: A Computational Model. Front Cell Neurosci 12, 191. [PubMed: 30061814]

Park JY, Dus M, Kim S, Abu F, Kanai MI, Rudy B, and Suh GSB (2016). Drosophila SLC5A11 Mediates Hunger by Regulating K(+) Channel Activity. Curr Biol 26, 1965–1974. [PubMed: 27397890]

Peyrache A, Lacroix MM, Petersen PC, and Buzsaki G (2015). Internally organized mechanisms of the head direction sense. Nat Neurosci.

Phillips-Portillo J (2012). The central complex of the flesh fly, Neobellieria bullata: recordings and morphologies of protocerebral inputs and small-field neurons. J Comp Neurol 520, 3088–3104. [PubMed: 22528883]

Renart A, Song P, and Wang XJ (2003). Robust spatial working memory through homeostatic synaptic scaling in heterogeneous cortical networks. Neuron 38, 473–485. [PubMed: 12741993]

Robinson MD, McCarthy DJ, and Smyth GK (2010). edgeR: a Bioconductor package for differential expression analysis of digital gene expression data. Bioinformatics 26, 139–140. [PubMed: 19910308]

Scheffer LK, Xu CS, Januszewski M, Lu Z, Takemura S. y., Hayworth KJ, Huang GB, Shinomiya K, Maitin-Shepard J, Berg S, et al. (2020). A Connectome and Analysis of the Adult Drosophila Central Brain. bioRxiv, 2020.2004.2007.030213.

Schlegel P, Texada MJ, Miroschnikow A, Schoofs A, Huckesfeld S, Peters M, Schneider-Mizell CM, Lacin H, Li F, Fetter RD, et al. (2016). Synaptic transmission parallels neuromodulation in a central food-intake circuit. Elife 5.

Seeholzer A, Deger M, and Gerstner W (2019). Stability of working memory in continuous attractor networks under the control of short-term plasticity. PLoS computational biology 15, e1006928. [PubMed: 31002672]

Seelig JD, Chiappe ME, Lott GK, Dutta A, Osborne JE, Reiser MB, and Jayaraman V (2010). Two-photon calcium imaging from head-fixed Drosophila during optomotor walking behavior. Nat Methods 7, 535–540. [PubMed: 20526346]

Seelig JD, and Jayaraman V (2013). Feature detection and orientation tuning in the Drosophila central complex. Nature 503, 262–266. [PubMed: 24107996]

Seelig JD, and Jayaraman V (2015). Neural dynamics for landmark orientation and angular path integration. Nature 521, 186–191. [PubMed: 25971509]

Shiozaki HM, and Kazama H (2017). Parallel encoding of recent visual experience and self-motion during navigation in Drosophila. Nat Neurosci 20, 1395–1403. [PubMed: 28869583]

Skaggs WE, Knierim JJ, Kudrimoti HS, and McNaughton BL (1995). A model of the neural basis of the rat's sense of direction. Adv Neural Inf Process Syst 7, 173–180. [PubMed: 11539168]

Soumillon M, Cacchiarelli D, Semrau S, van Oudenaarden A, and Mikkelsen TS (2014). Characterization of directed differentiation by high-throughput single-cell RNA-Seq. bioRxiv, 003236.

Stone T, Webb B, Adden A, Weddig NB, Honkanen A, Templin R, Wcislo W, Scimeca L, Warrant E, and Heinze S (2017). An Anatomically Constrained Model for Path Integration in the Bee Brain. Curr Biol.

Su TS, Lee WJ, Huang YC, Wang CT, and Lo CC (2017). Coupled symmetric and asymmetric circuits underlying spatial orientation in fruit flies. Nat Commun 8, 139. [PubMed: 28747622]

Sun Y, Nern A, Franconville R, Dana H, Schreiter ER, Looger LL, Svoboda K, Kim DS, Hermundstad AM, and Jayaraman V (2017). Neural signatures of dynamic stimulus selection in Drosophila. Nat Neurosci 20, 1104–1113. [PubMed: 28604683]

Talay M, Richman EB, Snell NJ, Hartmann GG, Fisher JD, Sorkac A, Santoyo JF, Chou-Freed C, Nair N, Johnson M, et al. (2017). Transsynaptic Mapping of Second-Order Taste Neurons in Flies by trans-Tango. Neuron 96, 783–795 e784. [PubMed: 29107518]

Taube JS (2007). The head direction signal: Origins and sensory-motor integration. Annual Review of Neuroscience 30, 181–207.

Taube JS, Muller RU, and Ranck JB (1990a). Head-direction cells recorded from the postsubiculum in freely moving rats. 1. Description and quantitative analysis. Journal of Neuroscience 10, 420–435. [PubMed: 2303851]

Taube JS, Muller RU, and Ranck JB (1990b). Head-direction cells recorded from the postsubiculum in freely moving rats. 2. Effects of environmental manipulations. Journal of Neuroscience 10, 436–447. [PubMed: 2303852]

Thurmond J, Goodman JL, Strelets VB, Attrill H, Gramates LS, Marygold SJ, Matthews BB, Millburn G, Antonazzo G, Trovisco V, et al. (2019). FlyBase 2.0: the next generation. Nucleic Acids Res 47, D759–D765. [PubMed: 30364959]

Triphan T, Poeck B, Neuser K, and Strauss R (2010). Visual targeting of motor actions in climbing Drosophila. Curr Biol 20, 663–668. [PubMed: 20346674]

Turner-Evans D, Wegener S, Rouault H, Franconville R, Wolff T, Seelig JD, Druckmann S, and Jayaraman V (2017). Angular velocity integration in a fly heading circuit. Elife 6.

Valerio S, and Taube JS (2012). Path integration: how the head direction signal maintains and corrects spatial orientation. Nature Neuroscience 15, 1445–1453. [PubMed: 22983210]

Varga AG, and Ritzmann RE (2016). Cellular Basis of Head Direction and Contextual Cues in the Insect Brain. Curr Biol 26, 1816–1828. [PubMed: 27397888]

Vitzthum H, Muller M, and Homberg U (2002). Neurons of the Central Complex of the Locust Schistocerca gregaria are Sensitive to Polarized Light. J Neurosci 22, 1114–1125. [PubMed: 11826140]

Wolff T, Iyer NA, and Rubin GM (2015). Neuroarchitecture and neuroanatomy of the Drosophila central complex: A GAL4-based dissection of protocerebral bridge neurons and circuits. J Comp Neurol 523, 997–1037. [PubMed: 25380328]

Wolff T, and Rubin GM (2018). Neuroarchitecture of the Drosophila central complex: A catalog of nodulus and asymmetrical body neurons and a revision of the protocerebral bridge catalog. J Comp Neurol 526, 2585–2611. [PubMed: 30084503]

Wu S, and Amari S (2005). Computing with continuous attractors: stability and online aspects. Neural Comput 17, 2215–2239. [PubMed: 16105223]

Wu S, Hamaguchi K, and Amari S (2008). Dynamics and computation of continuous attractors. Neural Comput 20, 994–1025. [PubMed: 18085986]

Xia S, Miyashita T, Fu TF, Lin WY, Wu CL, Pyzocha L, Lin IR, Saitoe M, Tully T, and Chiang AS (2005). NMDA receptors mediate olfactory learning and memory in Drosophila. Curr Biol 15, 603–615. [PubMed: 15823532]

Xie X, Hahnloser RH, and Seung HS (2002). Double-ring network model of the head-direction system. Phys Rev E Stat Nonlin Soft Matter Phys 66, 041902. [PubMed: 12443230]

Xie X, Tabuchi M, Brown MP, Mitchell SP, Wu MN, and Kolodkin AL (2017). The laminar organization of the Drosophila ellipsoid body is semaphorin-dependent and prevents the formation of ectopic synaptic connections. Elife 6.

Xu CS, Januszewski M, Lu Z, Takemura S. y., Hayworth KJ, Huang G, Shinomiya K, Maitin-Shepard J, Ackerman D, Berg S, et al. (2020). A Connectome of the Adult Drosophila Central Brain. bioRxiv, 2020.2001.2021.911859.

Yoganarasimha D, Yu XT, and Knierim JJ (2006). Head direction cell representations maintain internal coherence during conflicting proximal and distal cue rotations: Comparison with hippocampal place cells. Journal of Neuroscience 26, 622–631. [PubMed: 16407560]

Young JM, and Armstrong JD (2010). Structure of the adult central complex in Drosophila: Organization of distinct neuronal subsets. Journal of Comparative Neurology 518, 1500–1524.

Zhang K (1996). Representation of spatial orientation by the intrinsic dynamics of the head-direction cell ensemble: A theory. Journal of Neuroscience 16, 2112–2126. [PubMed: 8604055]

Zhang W, Basile AS, Gomeza J, Volpicelli LA, Levey AI, and Wess J (2002). Characterization of central inhibitory muscarinic autoreceptors by the use of muscarinic acetylcholine receptor knock-out mice. J Neurosci 22, 1709–1717. [PubMed: 11880500]

Zhang Z, Li X, Guo J, Li Y, and Guo A (2013). Two clusters of GABAergic ellipsoid body neurons modulate olfactory labile memory in Drosophila. J Neurosci 33, 5175–5181. [PubMed: 23516283]

Zheng Z, Lauritzen JS, Perlman E, Robinson CG, Nichols M, Milkie D, Torrens O, Price J, Fisher CB, Sharifi N, et al. (2018). A Complete Electron Microscopy Volume of the Brain of Adult Drosophila melanogaster. Cell 174, 730–743 e722. [PubMed: 30033368]

Zorita E, Cusco P, and Filion GJ (2015). Starcode: sequence clustering based on all-pairs search. Bioinformatics 31, 1913–1919. [PubMed: 25638815]

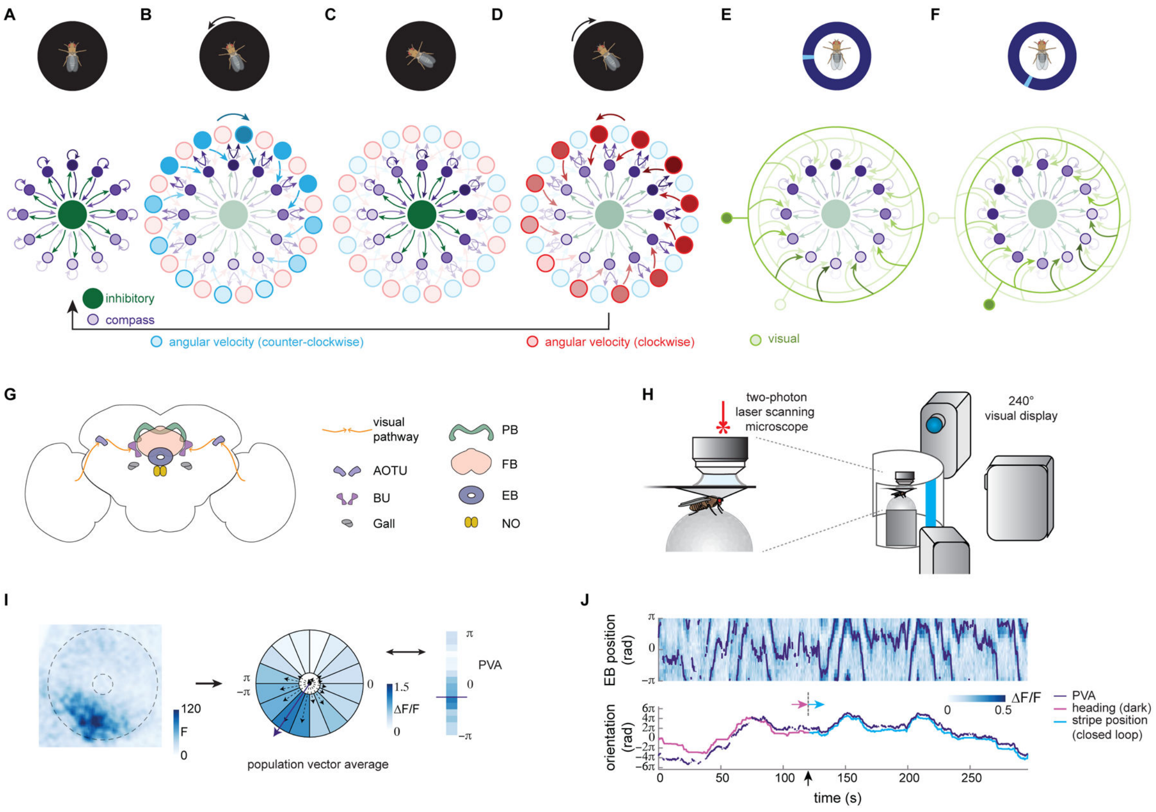

Figure 1: The fly neural compass as a ring attractor network

A–F: Function of the fly compass network schematized as a ring attractor in which the activity in each neuron is driven by excitatory angular velocity signals and inhibitory input from visual feature detectors. Darker shading indicates increased activity (the "bump"). The fly's behavior and visual environment (shown in the cartoons on top) activate different subpopulations within the compass network.

A. In the dark, local excitation (depicted for compactness as self-excitation) between compass neurons (purple) and uniform inhibition through inhibitory neurons (green, inside) leads to the formation of a 'bump' of activity that represents the fly's heading direction (here "north").

B. Active compass neurons excite paired neurons that conjunctively tune to both heading and angular velocity. When the fly turns counterclockwise (CCW), the CCW angular velocity neurons (blue), in turn, excite compass neurons, shifting their activity clockwise (CW) (dark blue arrow, top).

C. Shifted excitation from CCW angular velocity neurons moves the activity bump CW around the ring of compass neurons (dark purple).

D. When the fly instead turns CW, the CW angular velocity neurons (red) shift the activity bump in the CCW direction (dark red arrow, top).

E. Visual cues excite inhibitory visual feature detector neurons (green, outer ring) that suppress activity at all but a subset of compass positions. Here, a stripe at 9 o'clock activates a single visual neuron, which inhibits compass neuron activity everywhere except around 12 o'clock.

F. When the visual cue (here a single stripe) moves, a new visual feature detector is excited. Here, a stripe at 7 o'clock excites a feature detector that permits compass neuron activity at 10 o'clock.

G. A schematic of the fly central brain, focusing on a brain region called the central complex. The visual pathway into the central complex is shown with the orange arrows and progresses from the Anterior Optical Tubercle (AOTU) to the bulb (BU) and from the BU to the Ellipsoid Body (EB). Heading direction system neurons also arborize in the Gall, Protocerebral Bridge (PB), and Noduli (NO). The Fan-Shaped Body (FB) is the other central complex structure shown.

H. Calcium activity of different neuron types in the compass network was measured in a head-fixed preparation. (left) Genetically expressed calcium indicators were imaged using two-photon laser scanning microscopy while a fly walked freely on an air-suspended Styrofoam ball. The ball rotation was monitored to track the fly's orientation. (right) Visual stimuli (here, a 15° wide vertical stripe) were projected onto a 240° cylindrical screen with 3 projectors. Stimuli were either shown in open-loop (fly had no control of stimuli) or in one-dimensional closed-loop (the fly's turns on the ball changed the angular position of the stimulus).

I. (left) Fluorescence signal from GCaMP6f (here, in the E-PG neurons) showing the activity bump in the EB (the EB is outlined with the dotted lines). (middle) The EB is divided into 16 equiangular sectors of interest corresponding, approximately, to E-PG arborization patterns. The change in fluorescence ($\Delta F/F$) signal is then calculated in each of these regions. $\Delta F/F$ is, in turn, used to calculate the Population Vector Average (PVA) to estimate the bump position. (right) A snapshot of $\Delta F/F$ and the PVA at one moment in time.

J. (top) E-PG EB activity over time during an example trial. For the first 120 s, the fly is in darkness. For the final 150 s, the fly controls the angular position of a stripe in closed loop. The PVA is overlaid in purple. (bottom) The unwrapped PVA (purple), the heading in the dark (magenta), and the stripe position (blue) are shown. The bump tracks the fly's movements with accumulating error in darkness (before dotted line), and with minimal error in visual closed loop with a stripe stimulus (after dotted line).

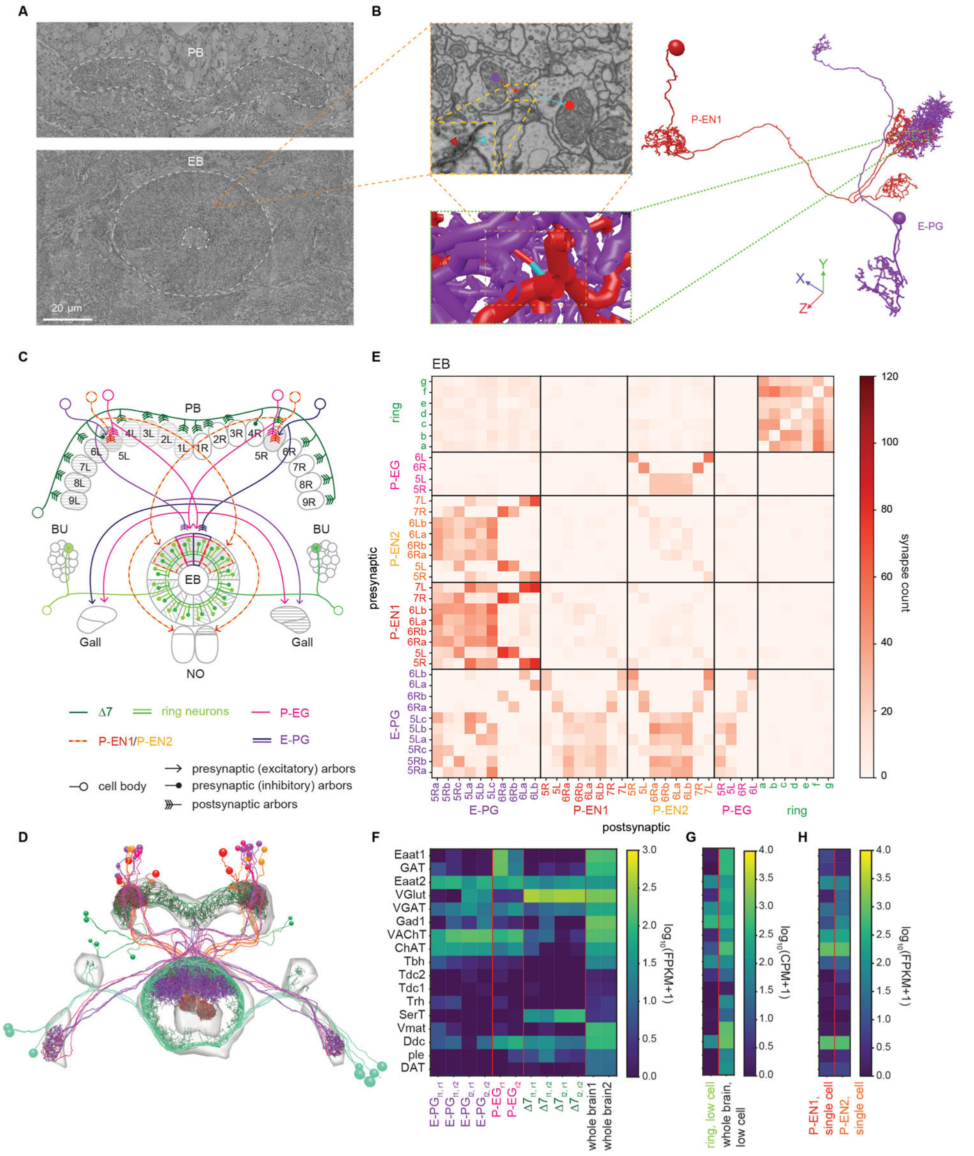

Figure 2: Electron-microscopic reconstruction and expression profiles of cellular components of compass network

A. Cross-sections of the FAFB electron microscopic volume showing the PB (top) and the EB (bottom).

B. An example synapse between an E-PG neuron (purple) and a P-EN1 neuron (red) in the EB. (top left) Electron microscopy cross-section from a region in the approximate location depicted by the box in Figure 2A (the actual location was from a slightly more posterior section). The inset shows a t-bar (red caret) and postsynaptic density (blue caret). (bottom left) Projected view of the 3D skeletons showing the synapse location between partners. (right) Complete skeletons of the two neurons showing the synapse location.

C. Schematic showing examples of neurons that are thought to play a role in the heading direction ring attractor. Neurons are color coded according to their putative roles in the attractor as shown in Figure 1A–F. Individual neurons are labeled according to where they arborize in the PB, following the numbering scheme here. Columnar neurons (E-PGs, P-ENs, and P-EGs) link subregions of the EB and PB while tangential neurons (Δ7s and ring neurons) arborize throughout either the PB or EB.

D. Skeletons of the subset of neurons that were manually traced in the FAFB dataset. Synapses were manually annotated but are not shown. The light gray regions show the outlines of the central brain neuropil. The neurons are colored as in Figure 2C.

E. Connectivity matrix for the traced neurons in the EB.

F–H. RNA sequencing was performed on the cell classes identified in Figure 2C. Genes related to transmitters are shown here. Three types of sequencing pipelines were used: bulk (F), low cell (G), and single cell (H) (See STAR Methods).

F. Bulk cell sequencing of E-PG, P-EG, and Δ7 neurons along with whole brain samples. l1 and l2 refer to distinct genetic lines while r1 and r2 refer to distinct technical replicates.

G. Low cell sequencing was performed on the ring neurons and on whole brain samples. The mean signal across biological replicates (7 for the ring neuron line and 8 for the whole brain material) is shown here.

H. Single cell sequencing was performed on the P-EN1 and P-EN2 genetic lines, which contained additional cell types. The mean signal across the samples is shown here.

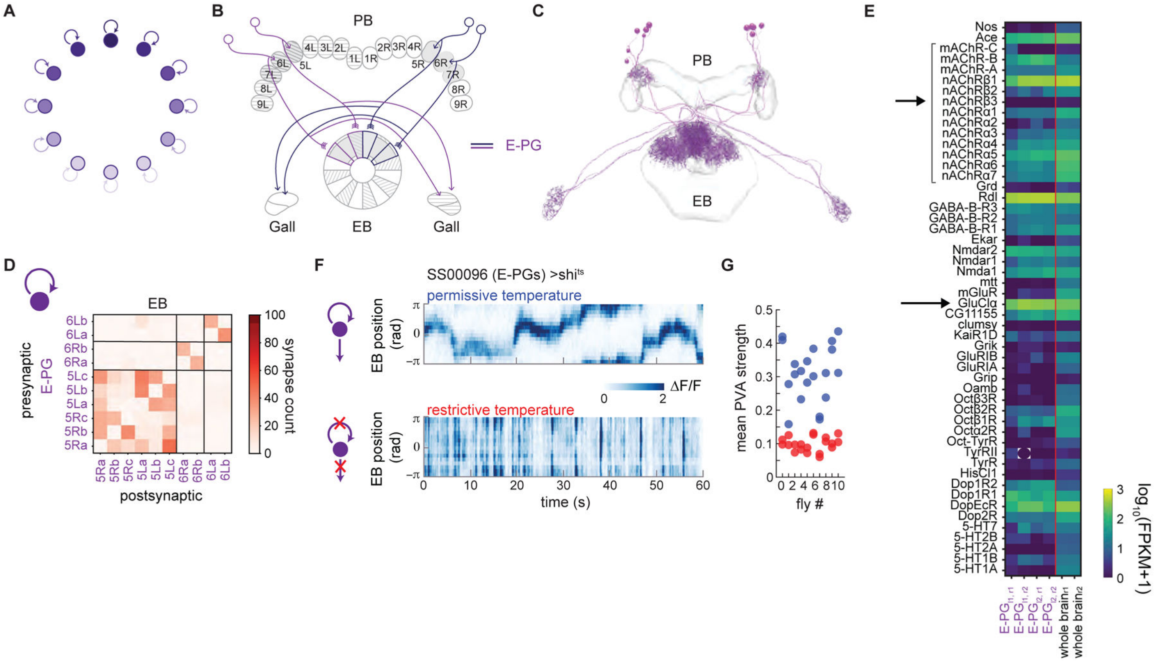

Figure 3: Local excitation from E-PGs is required to stabilize the E-PG activity bump

A. Local excitation reinforces the persistence of a bump of activity (dark purple).

B. Schematic depicting a subset of the E-PG neurons corresponding to those traced in the FAFB volume (Figure 3C). Gray shading shows areas of PB and EB in which the neurons were traced.

C. Putative excitatory (purple, E-PGs) neurons were traced and their synapses onto one another annotated.

D. Connectivity matrix within the ellipsoid body (EB). The E-PGs within a wedge are densely interconnected. Some E-PGs also make a few synapses onto their counterparts from neighboring wedges.

E. Expression of genes linked to receptors as compiled from RNA sequencing of the E-PGs and whole brain tissue (see STAR Methods). mRNA expression of nAChRs is highlighted, as is expression of the GluClα subunit.

F. Calcium activity in the ellipsoid body of the E-PGs as recorded with GCaMP6f for a fly expressing shi^{ts} in the E-PGs (SS00096). The fly is walking in darkness. At room temperature (top), a bump of activity is clearly visible. At the restrictive temperature (bottom), when synaptic vesicle reuptake is blocked within the E-PGs, the bump is no longer visible. Instead, E-PGs across the entire ellipsoid body flash off and on.

G. The PVA strength as a function of temperature across 10 flies. Restrictive temperature trials are shown in red, while permissive temperature trials are shown in blue. The PVA strength is the mean resultant vector length across the 16 ROIs that span the ellipsoid body (see Figure 1I). A PVA strength of 1 indicates that all of the activity is in one ROI, while a PVA strength of 0 indicates that the activity is spread equally across all ROIs. The average PVA strength for a given trial is shown.

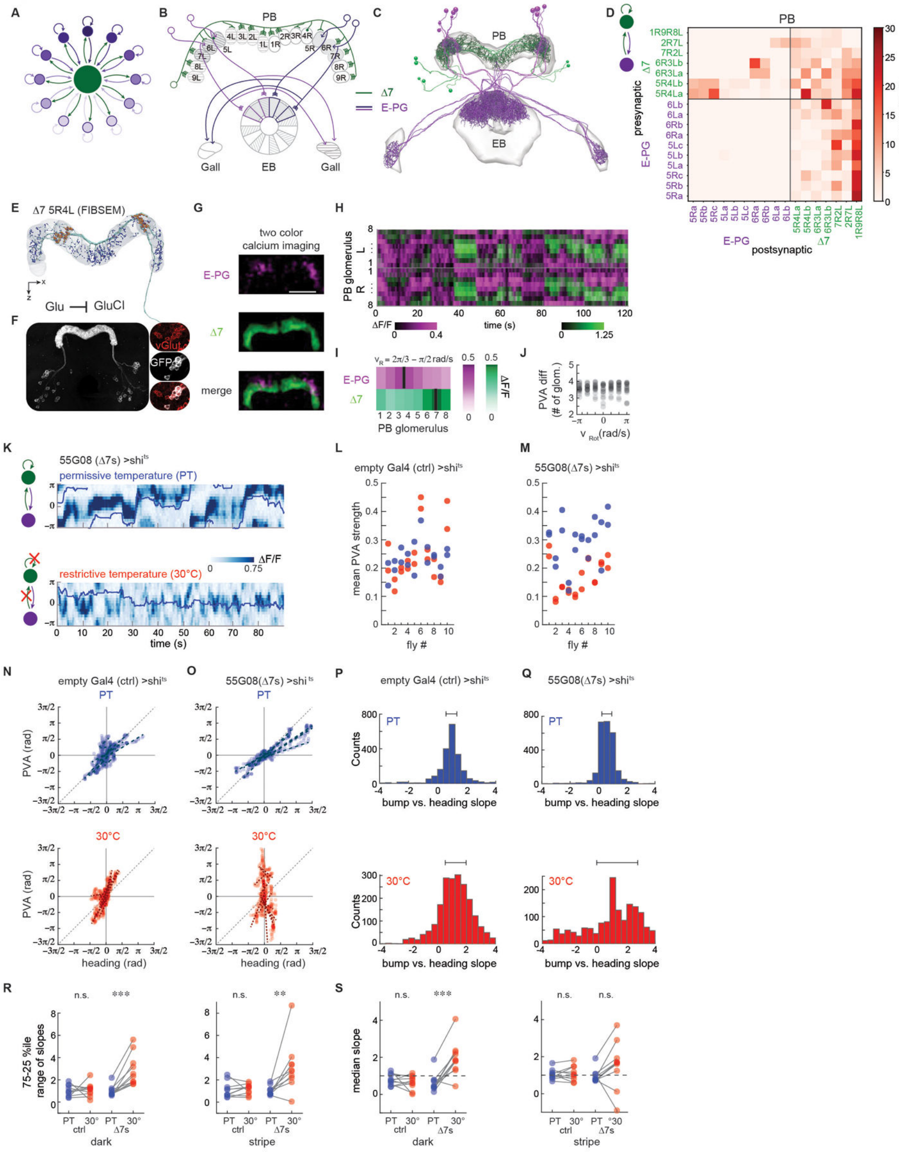

Figure 4: Long-range inhibition from Δ7s is required to stabilize the E-PG activity bump

A. Long-range inhibition helps maintain a single bump of activity (dark purple).

B. Schematic depicting a subset of the E-PG and Δ7 neurons corresponding to those traced (Figure 4C). Gray shading shows areas of PB and EB in which the neurons were traced. Note that Δ7s were also partially traced in other PB glomeruli to enable identification. Note that —in contrast to the schematized inhibition in A— Δ7 neurons do not synapse onto the E-PG neurons that they themselves receive input from.

C. Putative excitatory (purple, E-PGs) and inhibitory (green, Δ7s) neurons were traced and their synapses onto one another in the PB annotated.

D. Connectivity matrix within the protocerebral bridge (PB) for the E-PGs and Δ7s. The Δ7s synapse onto the subset of E-PGs within one glomerulus in the PB (5R→5R, 6R→6R, upper left quadrant) and receive broad input from the E-PGs away from that region (last column, lower right quadrant). The Δ7s synapse onto one another (upper right quadrant).

E. A single Δ7 neuron reconstruction (green) from the FIBSEM hemibrain connectome. Blue (postsynaptic) and orange (presynaptic) dots highlight synapses. Note that presynaptic specializations are localized to PB glomeruli separated by seven intermediate glomeruli (in this case, 5R and 4L).

F. Fluorescent *in situ* hybridization (FISH) of vGlut showed consistent overlap between GFP labeled Δ7s (white) and vGlut positive cells (red) (3/3 brains for the SS30295 genetic line and 2/2 brains for the SS02238 genetic line). (right) Glutamate release can lead to hyperpolarization of a downstream partner through GluCl channels.

G. Two-color calcium imaging was performed on the E-PGs (magenta) and the Δ7s (green) to record the simultaneous activity of the two populations. Here, GCaMP6f was expressed in the Δ7s and jRGECOla was expressed in the E-PGs.

H. The PB activity of both populations over time for the fly shown in I. The right and left PB were each divided into eight regions of interest (ROI), each corresponding to one glomerulus. The change in fluorescence intensity, ΔF/F, was then calculated for each ROI over time.

I. At each point in time, the red and green activity profiles were circularly shifted by the same number of ROIs in order to consistently place the peak of red activity at ROI #4. The mean registered activity in the right half of the PB across all time points when the fly in H was rotating at between $2\pi/3$ and $\pi/2$ rad/s is shown.

J. The PVA difference between E-PG and Δ7 activity as a function of rotational velocity, v_{Rot}. Data from 10 flies is shown, with both the right and left PB included. In 5 flies, GCaMP6f was expressed in the Δ7s and jRGECO1a was expressed in the E-PGs, while 5 flies had the reverse indicator expression pairing.

K. E-PG calcium activity in the ellipsoid body recorded with GCaMP6f in flies expressing shi^{ts} in the Δ7s (line 55G08) at permissive (top) and restrictive temperatures (bottom). The fly was presented with a stripe in closed loop over the course of the trial, and its position over time is indicated by the blue line.

L. In control flies, E-PG PVA strength at the permissive temperature (blue dots) and at the restrictive temperature (red dots) does not differ significantly ($p = 0.98$, paired t-test).

M. E-PG PVA strength is reduced at the restrictive temperature when vesicle reuptake is blocked at Δ7 synapses ($p = 2.8E-6$, paired t-test).

N. For 5 s sliding windows (see STAR Methods), the fly's position (heading) is plotted vs. the bump position (PVA). Blue dots indicate trials at the permissive temperature and red dots indicate trials at the restrictive temperature. Heading vs. PVA for 10 representative windows from an example control fly at the permissive (top) and restrictive (30 °C,bottom) temperatures. Each dotted line is a linear fit to the points within one window

O. Heading vs. PVA for an example fly expressing shi^{ts} in the Δ7s at the permissive (blue dots, top) and restrictive (red dots, bottom) temperatures.

P. The slope of the points in 5 s sliding windows. The two plots shown here are for flies expressing GCaMP6f in the E-PGs and shi^{ts} in empty Gal4 controls. The top plot shows a histogram of the slopes across two room temperature trials. The bottom plot shows a histogram of the slopes across three high temperature trials. The 25th and 75th percentiles are indicated above.

Q. As in Figure 4P, but now for flies expressing shi^{ts} in the Δ7s.

R. The range of slopes between the 25th and 75th percentiles, as obtained from the histogram of slopes, for the flies expressing shi^{ts} in empty Gal4 (ctrl) and the Δ7s. (left) The percentile range when the flies are in the dark. (right) The percentile range when the flies are tracking a closed loop stripe. Trials at the permissive temperature are in blue; trials at the restrictive temperature are in red. From left to right, p = 0.83, 4.8E-4, 0.78, and 9.7E-3 (paired t-test).

S. The median slope for the control flies in the dark (left) and with a stripe (right) for the room temperature trials (blue) and high temperature trials (red). From left to right, p = 0.61, 3.5E-4, 0.55, and 0.13 (paired t-test).

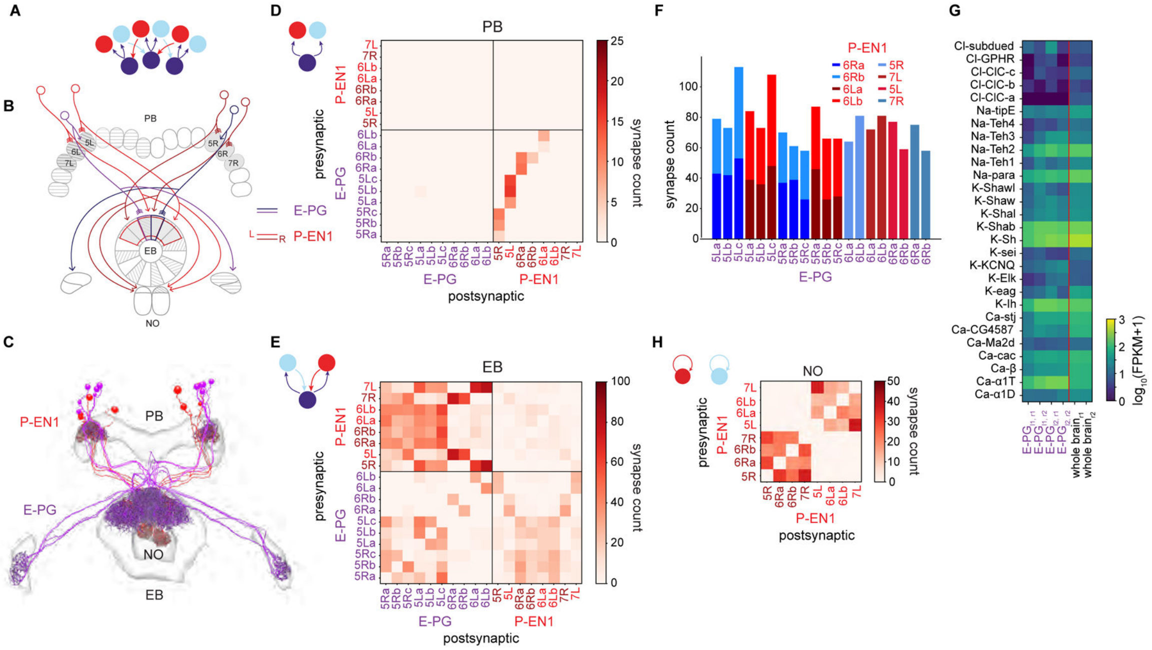

Figure 5: Recurrent loop between E-PGs and P-EN1s that updates bump position during turns is angularly shifted in the EB

A. Neurons that conjointly encode the fly's angular velocity and heading (red, light blue) move the bump (purple) around the ring (see Figure 1B).

B. Schematic displaying the anatomically-shifted recurrent loop between sample E-PGs and P-EN1s. EB wedges and PB glomeruli selected for E-PG and P-EN1 reconstruction (Figure 4C) are in gray.

C. E-PG and P-EN1 neurons were manually traced and their synapses onto each other annotated.

D. Connectivity matrix between the E-PGs and the P-EN1s in the PB. The E-PGs synapse onto the P-EN1s that arborize in the same glomerulus (lower right quadrant).

E. Connectivity matrix between the E-PGs and the P-EN 1s in the EB. The shifted P-EN 1s synapse onto the E-PGs (top left quadrant, e.g. P-EN1 6R→E-PG 5L). Note that the E-PGs also synapse onto the P-EN1s in the EB (bottom right quadrant).

F. The total number of synapses from P-EN1s onto individual E-PGs. Although some individual E-PGs receive inputs from single P-EN1s and others from two P-EN1s, the total number of synapses is approximately maintained ($p = 0.30$, two sample t-test, $n = 12$ samples for two P-EN1s, $n = 8$ samples for one P-EN1s).

G. mRNA expression of voltage-gated channels in the E-PGs.

H. Connectivity matrix between P-EN 1s in the NO. Note that P-EN 1s from the same side of the PB are heavily interconnected in the NO.

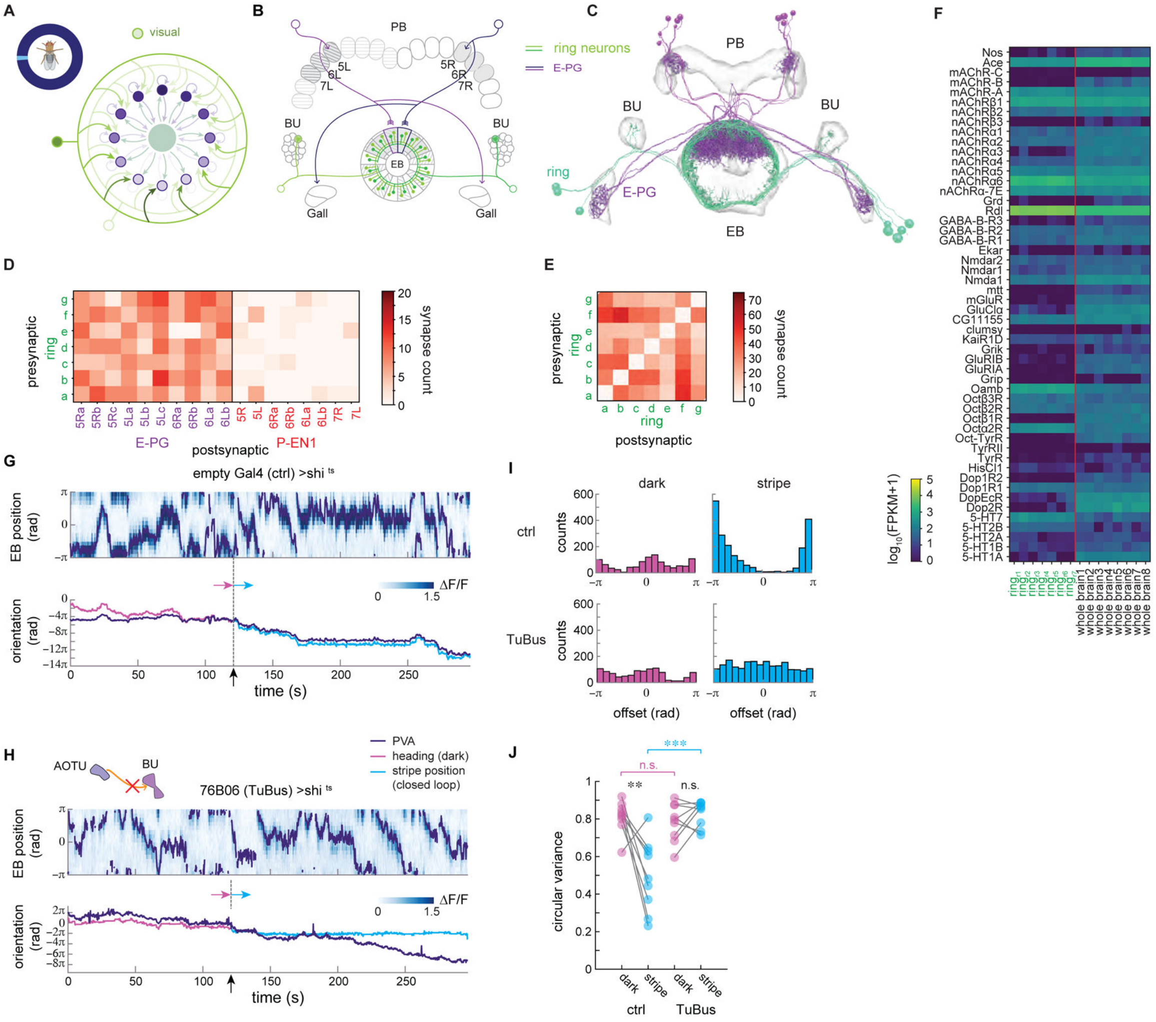

Figure 6: Mutually inhibitory R4d ring neurons synapse onto the E-PGs, tethering the bump to visual cues

A. Visual inputs (light green) map the visual scene onto the compass bump (dark purple) (see Figure 1E, 1F for details).

B. Schematic displaying ring neurons making synaptic contacts onto E-PGs in the EB. EB wedges and PB glomeruli selected for E-PG reconstruction (Figure 6C) are in gray.

C. R4d neurons (light green) were traced and their synapses onto each other and onto E-PG neurons (purple) were annotated.

D. Connectivity matrix between the E-PGs, P-EN1s, and ring neurons in the EB. This data is reproduced from Figure 2E.

E. Connectivity matrix between ring neurons in the EB. This data is reproduced from Figure 2E.

F. mRNA expression of receptor-linked genes for the ring neurons and whole brain tissue. Subscripts r1–r7 refer to biological replicates, each of which uses the same genetic line to target the R4d ring neurons.

G. (top) An example of E-PG EB activity over time for control flies at the restrictive temperature. The PVA is overlaid in purple. (bottom) Unwrapped PVA, heading in the dark, and stripe position over time. For the first 120 s, the fly is in darkness (heading shown in pink). For the final 150 s, the fly sees a stripe in closed loop (stripe position shown in light blue).

H.An example of E-PG EB activity for flies expressing shi^{ts} in the TuBu neurons at the restrictive temperature. Compare E-PG bump locking to visual cue movement when the fly is walking in closed loop with a stripe against that seen at permissive temperature (Figure 6G).

I. The offset between PVA and heading is calculated at each time point for the trials shown in Figure 6G and 6H, binned, and plotted here.

J. The circular variance for the offset distribution across flies in the dark and when a closed-loop stripe is present (p = 4.9E-3, 0.23 (paired t-test)). Mean of the circular variance is not significantly different between the control and TuBu flies in the dark (p = 0.69, two-sample t-test across genotypes). Circular variance between the control and TuBu flies is however significantly different in the presence of a stripe in closed loop (p = 2.9E-4, two-sample t-test across genotypes).

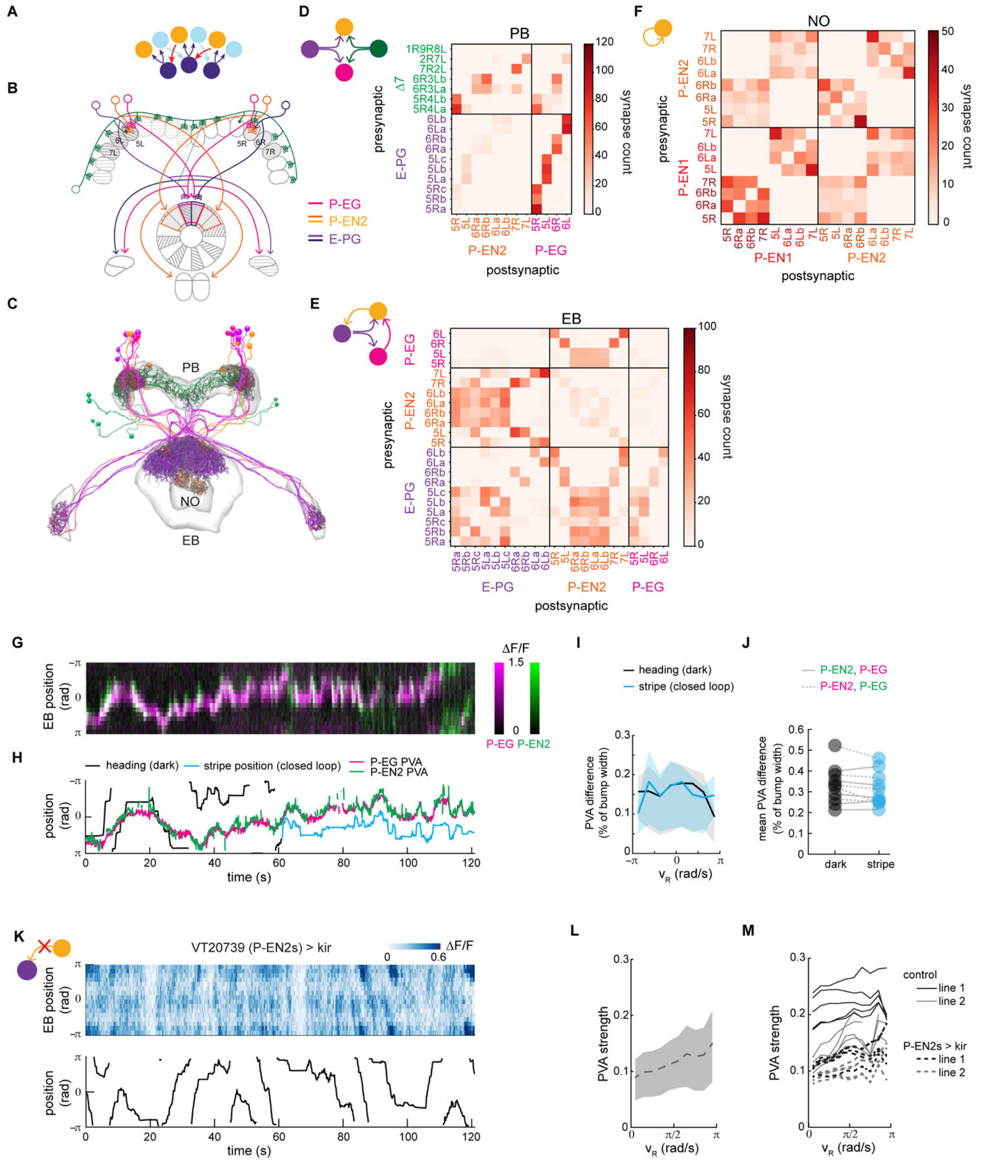

Figure 7: P-EG and P-EN2 neurons together create a second recurrent loop with E-PGs

A. P-EN2 neurons (orange and light blue), like P-EN1s (Figure 4), conjointly encode the fly’s heading and angular velocity, creating an angularly shifted recurrent loop with E-PGs (purple).

B. Schematic of P-EG and P-EN2 arborizations in the central brain. EB wedges and PB glomeruli selected for E-PG, P-EG and P-EN2 reconstruction (Figure 6C) are in gray.

C. Reconstructed E-PG, P-EG, Δ7 and P-EN2 neurons. Synapses were labelled between these neurons in the NO and Gall and in selected parts of the EB and PB (Figure 6B).

D. Connectivity matrix between the E-PGs and Δ7s and the P-EN2s and P-EGs in the PB. The E-PGs form a large number of synapses onto the P-EGs (lower right quadrant).

E. Connectivity matrix between the E-PGs, P-EN2s, and P-EGs in the EB. The P-EGs only synapse onto the P-EN2s (top middle).

F. Connectivity matrix between the P-EN2s and P-EN1s in the NO. Note that the P-EN 1s and P-EN2s are interconnected in each nodulus.

G. Two color calcium imaging of P-EG (magenta, labeled with jRGECO1a) and P-EN2 (green, labeled with GCaMP6f) activity in the EB for a fly in the dark.

H. The PVAs of P-EG and P-EN2 bumps of activity are shown along with the fly's heading in the dark (black trace) and the closed-loop stripe position when visible (blue trace).

I. Mean PVA difference across rotational velocities for the fly shown in Figure 7G, 7H. The upper and lower quartile range is shown in the shaded region.

J. Mean PVA difference across all velocities across flies in the dark or with a closed-loop stripe.

K. (top) Calcium activity in the E-PGs in the EB for a fly in the dark when the P-EN2 neurons express Kir. (bottom) The fly's heading over the duration of the trial.

L. The mean PVA strength of the calcium activity in the EB as a function of the fly's rotational velocity for the fly shown in H. The standard deviation is shown in the shaded region.

M. The PVA strength for 10 flies (5 for each genetic line) expressing Kir in the P-EN2s (dotted lines) relative to the control flies (solid lines) as a function of the fly's rotational velocity.

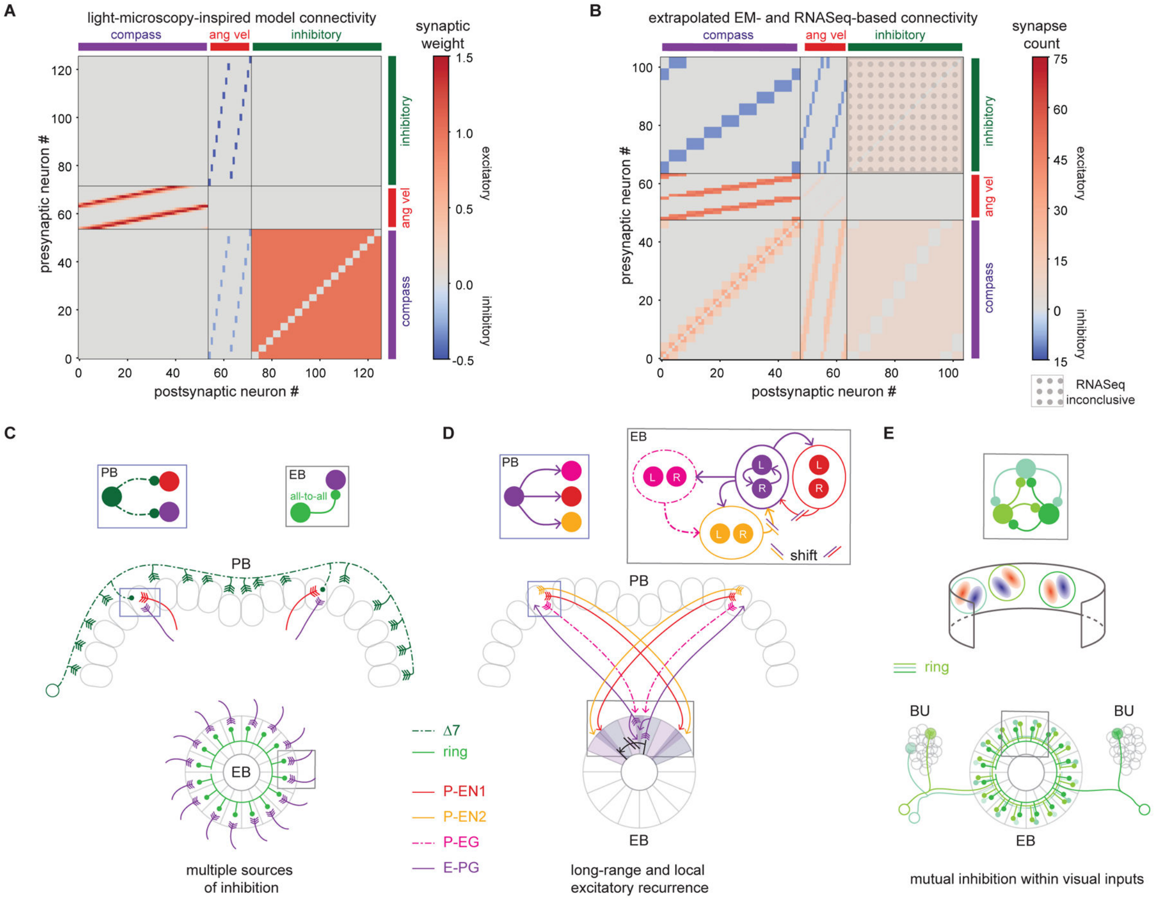

Figure 8: The fly ring attractor network is broadly consistent with theory, but also features unpredicted components and motifs

A. Weight matrix for previous theoretical ring attractor model (Turner-Evans et al., 2017) for the fly compass (see STAR Methods).

B. Connectivity matrix extrapolated from data presented in this work. The synapse counts from the EB and PB are averaged and extrapolated to all untraced neurons of every class. Excitatory connections are shown in red and inhibitory connections are shown in blue.

C. Inhibition within the fly ring attractor appears to stem from multiple neuron classes, including the Δ7s and ring neurons. The Δ7s provide more structured, long-range inhibition of E-PG and P-EN neurons with different heading tuning in the PB (middle row; expanded view in box at top left), and different classes of ring neurons provide more uniform inhibition of E-PGs in the EB (bottom row; expanded view in box at top right).

D. Recurrent excitation between neurons with similar heading tuning (‘local excitation’ in the context of ring attractor models) takes many forms. E-PGs from a specific wedge in the EB synapse onto P-ENs and P-EGs in the PB (schematized in bottom row and expanded into box at upper left). P-ENs project back onto the E-PGs in the EB synapsing onto E-PGs from neighboring tiles (shift shown in bottom row; expanded view in box at upper right). P-EGs also project back without a shift to the EB, where they synapse onto the P-EN2s (upper right). E-PGs also synapse onto P-ENs within the EB (upper right).

E. Visual input neurons (simplified receptive fields indicated by red excitatory and blue inhibitory subfields in middle row) synapse onto one another in the EB (bottom row; expanded view in box at top). This mutual inhibition between visually responsive ring neurons may enable winner-take-all dynamics between visual cues, and/or gain control that maintains the same level of inhibition in the circuit in the presence of single or multiple visual cues.